

EXPERIMENTAL AND COMPUTATIONAL EVALUATION OF A VIBRATORY
FINISHING PROCESS

by

Jayesh Abhay Navare

A thesis submitted to the faculty of
The University of North Carolina at Charlotte
in partial fulfillment of the requirements
for the degree of Master of Science in
Mechanical Engineering

Charlotte

2017

Approved by:

Dr. Brigid Mullany

Dr. Russell Keanini

Dr. Peter Tkacik

Dr. Thomas Suleski

©2017
Jayesh Abhay Navare
ALL RIGHTS RESERVED

ABSTRACT

JAYESH ABHAY NAVARE. Experimental and computational evaluation of a vibratory finishing process. (Under the direction of DR. BRIGID A. MULLANY)

Vibratory finishing is among the widely recognized mass finishing techniques which is used for cleaning, deburring, edge rounding, polishing, and creating an isotropic surface finish on metal parts that have undergone previous machining operations. Despite this process being straightforward and easy to implement at a very low cost and with a good degree of automation, an understanding of the basic mechanics of material removal and surface modification mechanism is lacking. In this work the potential of treating the media as a fluid is explored and a continuum mechanics based approach is taken to model the flow of media around a stationary workpiece in a computational fluid dynamics (CFD) environment. Important aspects of CFD model design and analysis are discussed and CFD derived pressure and velocity distributions are used to explain the variations in surface finishes obtained on two aluminum workpieces that were subjected to different media flow conditions. The results outlined in this thesis demonstrate the potential of using a CFD modeling approach to predict the process outcomes, while also providing a solid foundation for further modeling efforts.

DEDICATION

To my mentor and an extraordinaire teacher, Dr. Brigid Mullany, for guiding and supporting me during my endeavor to become a better engineer.

ACKNOWLEDGEMENTS

The work presented here is built on the existing foundation laid down by the vibratory finishing group at UNC Charlotte lead by Dr. Brigid Mullany, Dr. Russell Keanini, and Dr. Peter Tkacik. I am extremely grateful for the support and guidance that I received from Dr. Brigid Mullany and Hossein Shahinian while working towards the completion of my Master's degree. I would like to extend my gratitude to Brian Dutterer and Joel Pritchard for teaching me invaluable machining skills and shop floor safety practices. Lastly, I would like to thank the MEES department at UNC Charlotte for supporting all my activities undertaken as a Graduate student.

TABLE OF CONTENTS

LIST OF TABLES	xi
LIST OF FIGURES	xii
1 INTRODUCTION	1
2 BACKGROUND	3
2.1 Process kinematics	3
2.2 Process elements and their function	3
2.2.1 Media	4
2.2.2 Machine	4
2.2.3 Compound	5
2.3 Fundamental problem in vibratory finishing	6
2.4 Process metrics	7
2.4.1 Isotropic surface and smoother surface generation	7
2.4.2 Cleaning, deburring and material removal	7
2.5 Vibratory finishing research areas	8
2.6 Research efforts based on material removal	8
2.6.1 Media type	9
2.6.2 Bowl loading, process frequency, and acceleration	10
2.6.3 Workpiece fixturing	11
2.6.4 Workpiece material	13

2.6.5	Material removal models	13
2.7	Research efforts based on surface finishes	15
2.8	Research efforts using diagnostic tools that provide insights into process mechanics	17
2.8.1	Force sensors to measure impact loads and velocity	17
2.8.2	High speed imaging camera and application of PIV system to vibratory finishing	19
2.9	Research effort that treat granular media as a continuum fluid	20
2.10	Summary	21
3	CFD MODEL DESIGN AND COMPARISON TO EXPERIMENTAL CONDITIONS	23
3.1	Experimental flow measurement of vibrating media	23
3.1.1	Vibratory equipment and operating conditions	23
3.1.2	Particle image velocimetry (PIV) to measure media flow	24
3.2	CFD model implementation	26
3.2.1	CFD software package	27
3.2.2	Control volume and mesh generation	27
3.3	Inputs to CFD model	29
3.3.1	Media density	29
3.3.2	Dynamic viscosity	30
3.3.3	Inlet boundary velocities	31
3.3.4	Solution initialization and method	33

3.4	Comparison between CFD and PIV velocity field	33
3.5	CFD model sensitivity	34
3.5.1	CFD model sensitivity to dynamic viscosity	36
3.5.2	Model sensitivity to meshing style	37
3.5.3	Model sensitivity to meshing density	38
3.5.4	Model sensitivity to initialization of flow variables	41
3.6	Synopsis of CFD model sensitivity analysis	42
3.7	Summary	43
4	EXPERIMENTAL TESTING: SURFACE TOPOGRAPHY VARIATIONS RESULTING FROM MEDIA APPROACH ANGLES	45
4.1	Experimental setup	45
4.2	Workpieces	46
4.3	Testing conditions	47
4.4	PIV results and inputs to CFD model of media flow around the workpiece	48
4.5	Comparison of CFD predicted media velocity field with PIV measured velocity field	49
4.6	Material removal	52
4.7	Quantification of surface finishes	53
4.8	Surface finishes on aluminum workpieces	55
4.8.1	Test 1 – Tangential flow (Left surface)	56
4.8.2	Test 1 – Tangential flow (Right surface)	57

4.8.3	Test 2 – Normal flow (Upstream surface)	58
4.8.4	Test 2 – Normal flow (Downstream surface)	59
4.9	Summary	60
5	CORRELATION BETWEEN CFD MODEL OUTPUTS AND RESULTING WORKPIECE TOPOGRAPHY	62
5.1	Static pressure and tangential velocity profiles for Test 1 (tangential flow)	62
5.2	Static pressure and tangential velocity profile for Test 2 (normal flow)	63
5.3	Correlation between CFD metrics and experimentally observed workpiece topographies	64
5.4	CFD based predictions to find optimal location of workpiece placement in the flow field	65
5.5	Media-workpiece contact model to investigate surface features obtained after finishing	67
5.5.1	Radius of media edge	69
5.5.2	Normal load	70
5.5.3	Empirical correlation	71
5.6	Comparison of theoretical depth of indentation, h with the experimentally obtained depth of pit marks	72
5.7	Discussion of results	73
5.8	Summary	74
6	CONCLUSIONS AND FUTURE WORK	75
6.1	Summary of work to date	75
6.2	Future work	77
	PUBLICATION	79

REFERENCES	80
APPENDIX A: MATLAB CODE TO EXTRACT MEDIA VELOCITY FIELD FROM PIV RAW DATA	83
APPENDIX B: C PROGRAM TO LINK PIV VELOCITIES TO CFD MODEL	84
APPENDIX C: MATLAB CODE TO EVALUATE SURFACE FINISHES FROM RAW BINARY FILE	86
APPENDIX D: MATLAB CODE TO COMPARE CFD PREDICTED AND PIV MEASURED VELOCITIES	88
APPENDIX E: MATLAB CODE TO SEQUENTIALLY ARRANGE AS PER TIMESTAMP AND CONVERT HIGH SPEED IMAGES TO GRAYSCALE	91
APPENDIX F: MATLAB CODE TO SAVE PIV PROCESSED DATA AS A MATLAB M-FILE	92

LIST OF TABLES

Table 3.1 Media packing density	30
Table 3.2 Parameter sensitivity to model outputs	43
Table 4.1 Mass loss evaluation for analyzing material removal	53

LIST OF FIGURES

Figure 2.1 Media types [5]	5
Figure 2.2 The key process variables of vibratory finishing and the process outcomes. (Top right schematic from ref. [7])	6
Figure 2.3 Basic rules of vibratory finishing as stated by Hashimoto [8], and graphed by [9]	9
Figure 3.1 a) Experimental Setup, b) High Speed Camera FOV	25
Figure 3.2 PIV generated velocity vector map of media flow	25
Figure 3.3 Image for calibrating the PIV velocity vector map	26
Figure 3.4 Road map for CFD model implementation	28
Figure 3.5 a) Control volume for CFD analysis and b) Meshing	29
Figure 3.6 a) CFD inlet and outlet boundaries and b) solution initialization location	32
Figure 3.7 Experimental (PIV) and numerically evaluated (CFD) velocity component at a) Top edge, b) Left edge, and c) Right edge	32
Figure 3.8 PIV measured and CFD predicted velocity fields	35
Figure 3.9 Percentage error in a) velocity magnitude and b) velocity phase	35
Figure 3.10 Location of vertical line within the CFD control volume along which the velocity profile is evaluated for comparing changes in input parameters	36
Figure 3.11 Velocity distribution across the entire control volume for a range of dynamic viscosities	38
Figure 3.12 Velocity profiles for a range of dynamic viscosities	39
Figure 3.13 Velocity profile for different meshing styles	39
Figure 3.14 Velocity distribution across the control volume for different meshing styles	40
Figure 3.15 Velocity distribution across the control volume for coarse mesh and refined mesh	40

Figure 3.16 Velocity profile for coarse and refined mesh	41
Figure 3.17 Velocity profiles for different locations of flow variable initialization	42
Figure 3.18 Velocity distribution for different locations of flow variable initialization	43
Figure 4.1 Experimental setup. (Left) Tangential near – workpiece flow. (Right) Normally – impinging near – workpiece flow	46
Figure 4.2 Ground aluminum workpiece	48
Figure 4.3 Testing conditions. (Left) Tangential near – workpiece flow. (Right) Normally – impinging near – workpiece flow	48
Figure 4.4 Time - averaged media velocity field evaluated using PIV for (Left) Test 1- tangential flow and (Right) Test 2 – normal flow as depicted in Figure 4.3	49
Figure 4.5 Comparison between PIV measured and CFD predicted velocity fields for Test 1 tangential flow	50
Figure 4.6 Comparison between PIV measured and CFD predicted velocity fields for Test 2 normal flow	51
Figure 4.7 CFD predicted and PIV measured velocities: (a) Test 1, and (b) Test 2	52
Figure 4.8 Weighing scale to measure the amount of mass loss	53
Figure 4.9 (Left) Zygo ZeGage SWLI. (Right) Measurement locations.	54
Figure 4.10 Fixture for integrating linear and a rotary stage movements to align workpiece position	55
Figure 4.11 SWLI measurement on workpiece ‘Left’ surface for pre (a) and post Test 1 (b, c). See Figure 4.3 for workpiece surface naming convention	56
Figure 4.12 SWLI measurement on workpiece ‘Right’ surface for pre (a) and post Test 1 (b, c) indicating highest amount of pitting. See Figure 4.3 for workpiece surface naming convention	57
Figure 4.13 SWLI measurement on workpiece ‘Upstream’ surface for pre (a) and post Test 2 (b, c) indicating highest amount of surface smoothing. See Figure 4.3 for workpiece surface naming convention	59
Figure 4.14 SWLI measurement on workpiece ‘Downstream’ surface for pre (a) and post Test 2 (b, c). See Figure 4.3 for workpiece surface naming convention	60

Figure 5.1 CFD predicted flow variables for Test 1. (a) Predicted tangential velocity, and (b) Predicted static pressure	63
Figure 5.2 CFD predicted flow variables for Test 2. (a) Predicted tangential velocity, and (b) Predicted static pressure	63
Figure 5.3 a) Workpiece surface naming convention and workpiece orientation, b) CFD derived average static pressure at approximately 5 mm from workpiece surface for a given workpiece orientation, and c) CFD derived average tangential velocity at approximately 5 mm from workpiece surface for a given workpiece orientation.	67
Figure 5.4 Test 1 - Tangential flow schematic and workpiece surface naming convention	68
Figure 5.5 Indentation event created by media-workpiece contact	69
Figure 5.6 Evaluation of media edge radius. (a) line profile across the length of media edge obtained from SWLI measurement, and (b) Best-fit circle fitted to the line profile to obtain the media edge radius in μm	70
Figure 5.7 SWLI measurement of workpiece 'Right' surface. Slice 1 refers to a profile measurement across a 0.5 mm trace	73
Figure 5.8 SWLI measurement of workpiece 'Right' surface. Slice 2 refers to a profile measurement across a 0.5 mm trace	74

1 INTRODUCTION

Vibratory finishing and other types of mass finishing processes such as tumbling, drag finishing, spindle finishing, centrifugal disk, and centrifugal barrel finishing are commercially used to achieve a variety of surface effects such as deburring, polishing, compressive stresses, etc. on metals as well as components made from other materials. With the increasing industrial demands on surface finishes, these processes are finding increased application in finishing of high value components used in aeronautical and biomedical industry such as blisks, single turbine blades, and orthopedic implants. The basic kinematics of vibratory finishing process involves placing millimeter size pellets also known as media, workpiece(s), and a compound (typically a combination of chemicals that dissolve in water and form solutions to enhance the action of media [1]) into a vibrating container. The vibrational energy transferred to the media through container walls causes the media to achieve steady state flow conditions within the container. The relative motion between the media and the workpiece entrained within the media results in material removal and/or surface modification depending upon the nature of media – workpiece contact [2].

Providing good degree of automation, creating isotropic surface finish, and improving the workpiece fatigue life are among the reasons for the increasing popularity of this process [1].

Thus, understanding the functional relationship between the process variables, e.g. frequency and amplitude of vibration, and the process outcomes such as material removal rate and surface finish can have a positive impact on the manufacturing industry.

An important aspect of this project is to design and develop a continuum based numerical model replicating the flow of media around stationary workpieces in a computational fluid dynamic (CFD) environment by treating the media as a Newtonian fluid. In order to validate the model, CFD predicted velocity profiles are compared to the velocity profiles of media flow around stationary workpieces as measured via particle image velocimetry (PIV). The predicted local pressures and local velocities are considered for explaining the measured variations in workpiece surface topographies.

An overview of past modelling approaches, empirical investigations pertaining to vibratory finishing, and justification for treating the media as a fluid are given in Chapter 2. Chapter 3 outlines the design and development of a CFD model and compares the predicted velocity fields to the PIV measured velocity fields. Chapter 4 describes the experimental testing conditions and evaluation of process metrics, while Chapter 5 discusses the correlation between CFD predicted outputs and experimentally measured variations in workpiece surface finishes. Lastly, in Chapter 6, conclusions from the current work and proposed future work are outlined.

2 BACKGROUND

This chapter gives an overview of vibratory finishing processes, from basic kinematics of the process to advanced developments pertaining to material removal models and empirical investigations. Various research attempts to understand the mechanics of material removal in vibratory finishing are studied and a brief summary of each is outlined in the following sections. The significance of this process in the aviation, biomedical, and automobile industry is discussed and various process parameters and their functions are listed.

2.1 Process kinematics

The kinematics of a vibratory finishing process involves an unbalanced motor that generates vibrations within the container that holds the media and the workpiece. The vibrations induced in the container are transferred to the media through the container walls and causes the media to go into a steady state flow pattern. The relative motion between the media and the workpiece entrained within the media leads to material removal and/or surface modification.

2.2 Process elements and their function

The important process elements that govern the vibratory finishing processes are media, compound, and the machine (equipment). For a given application, the proper selection of these elements plays a very crucial role and therefore it is important to understand the function of each and every element.

According to [3], these elements are interdependent on each other to such an extent that if anyone of them fails then the entire process fails. The function of the various process elements are as follows:

2.2.1 Media

Media is the crucial parameter that imparts the desired surface finish on the workpieces. Typically media (see Figure 2.1) are stones or pellets that can be made from a range of materials such as ceramics, polymers, metals, or even organic (e.g. corn cobs) and can have triangular, cylindrical, or pyramidal shapes with sizes up to about 25 mm [1], [4]. The shape and material of media is very important with respect to the process outcomes. For example, a spherical ceramic media is typically used in applications where critical surface finish is desired while spherical steel balls are used to induce compressive stresses in workpieces [1]. The shape, size, and material of the media effectively contribute to the relative velocity between the media and the workpiece which in turn governs the material removal mechanism. Thus it is seen that there are a wide range of options for selecting the media and depending on the type of application, the user has to make a choice that best fits the application.

2.2.2 Machine

Depending upon the size of the workpiece that needs to be finished, the vibratory finishing equipment can vary in shape (bowl, tub or trough) and capacity. The flow pattern of media inside the vibratory finisher is governed by the eccentric weights attached to the motor which are responsible for inducing vibrations into the container. The frequency of vibration (Hz) or the motor speed (rpm) which is one of the motor specifications is selected based on the type of application and can be altered by changing the driving voltage. The

amplitude of vibration depends upon the motor speed and the mass of the eccentric weights and for most systems is usually 2 ~ 5 mm.

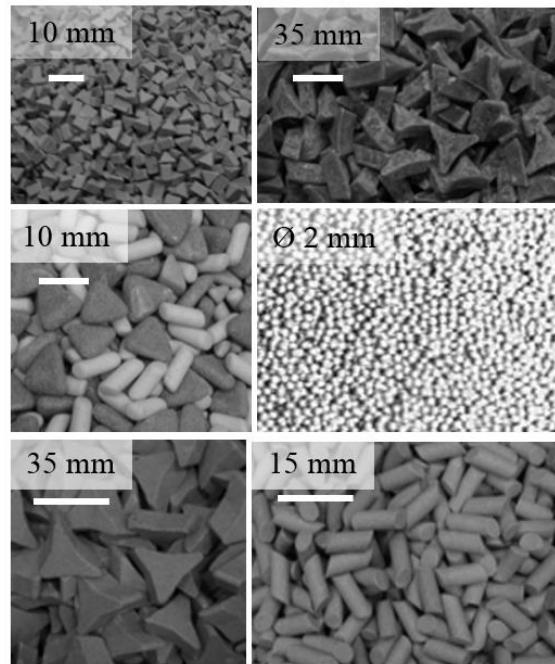


Figure 2.1 Media types [5]

2.2.3 Compound

As described by [1], compound is typically a combination of chemicals that dissolve in water and form solutions to enhance the action of media against the workpieces. The proportion of compound used in vibratory machine is an important factor that needs to be considered as it can facilitate in effective cutting of material or it can only clean the workpiece surfaces [3]. Care needs to be taken in deciding the correct proportion of compound to be used as too much of it will lead to a cushioning effect between the media and the workpiece and reducing process efficiency [3]. Apart from cleaning the workpiece surface and aiding in cutting action, another important function of the compound is to suspend the media and workpiece particulates (chips) and prevent them from depositing on the workpiece surface [3]. In some applications, the compound solution is used to apply

inhibitors on workpiece surfaces thereby preventing them from corrosion while in almost all applications it is used to absorb heat generated during rubbing of media against the workpieces [3].

2.3 Fundamental problem in vibratory finishing

The complexity of this process is realized when the number of specifications associated with the above mentioned process elements are considered (see Figure 2.2) [6]. While the user selects any of the process variables, due to lack of scientific knowledge about the mechanism of material removal, the user often resorts to trial and error approaches in order to get the desired outcome.

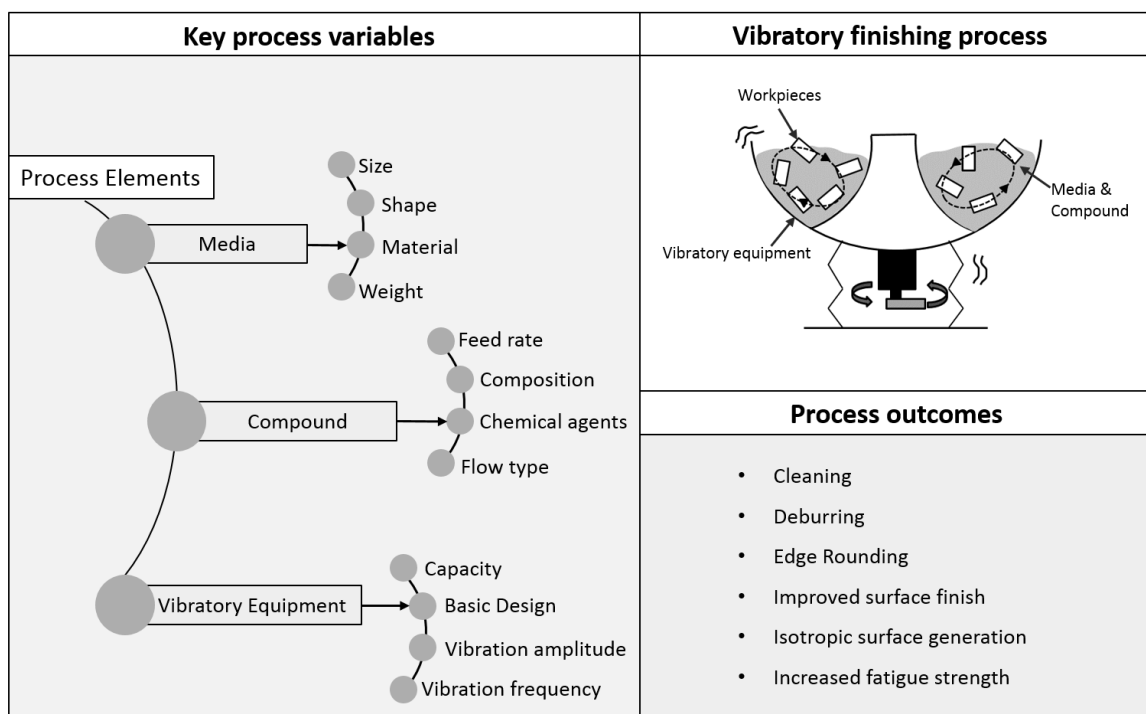


Figure 2.2 The key process variables of vibratory finishing and the process outcomes. (Top right schematic from ref. [7])

2.4 Process metrics

Vibratory finishing is implemented on parts that have undergone previous machining operations with a goal to condition the surface features and obtain an isotropic finish. The following provides a description of the various process metrics.

2.4.1 Isotropic surface and smoother surface generation

One of the reasons that makes vibratory finishing such a popular process is its application in creating isotropic and smoother surfaces. The interaction between the media and the workpiece leads to material removal or surface modification. The tool path marks on parts that have been previously machined are removed and replaced with a non-directional uniform surface finish. Vibratory finishing tends to improve the surface roughness over the period of processing time which is a very significant outcome for parts that are used in aviation (blisks, impeller, turbine blades) and biomedical (dental implants, knee joints, hip joints) industry. Empirical investigations by [8] indicate that vibratory finishing process has a roughness limitation that depends on the process elements and an exponential decay in the surface roughness values is observed after a certain time interval.

2.4.2 Cleaning, deburring and material removal

Vibratory finishing is widely employed for deburring and cleaning of parts and compared to hand deburring (filing) has a lower cost and takes minimal efforts to remove burrs. The size, shape, and the material of media used dictates the amount of deburring and material removal. Bigger media particles provide a higher depth of cut and thereby facilitate in higher material removal or surface modification rates [3]. Ceramic media is usually preferred in applications where material removal is required while steel, plastic, or even organic media are used for cleaning and burnishing applications.

2.5 Vibratory finishing research areas

Numerous approaches have been taken to understand the mechanics of material removal and surface modification. Most of these approaches are empirical investigations and are mostly confined to a specific application of vibratory finishing. Although a few material removal models are available in the literature, the mechanism behind vibratory finishing still remains unclear. Hashimoto [8] established three fundamental rules of vibratory finishing. The first rule states that the process has an inherent surface texture and a roughness limitation that is reached after a certain process time. The limitation will be a function of process parameters and media selection. The second rule states that the change in surface roughness with time is proportional to the difference in surface roughness at a given time and the roughness limitation. The third rule explains about the material removal rate and states that a constant material removal rate occurs after the steady state process is reached. The empirical model postulated by Hashimoto, for a given set of parameters and consumables, not only predicts the surface roughness of components at a given process time but also finds the optimum process time beyond which improvement in roughness is not feasible. If any of the process parameters change the new limits and time constants will be required. This can only be obtained via experimental work. The summary of the three rules is graphically represented in Figure 2.3. Some of the research efforts pertaining to material removal, surface finishes, and diagnostic tools that provide insights into the process are summarized in the following sections.

2.6 Research efforts based on material removal

This section details about the various factors that affect the material removal rate with reference to empirical investigations and model developments undertaken by several

researchers. The main contributors to material removal rate that are discussed include media type, bowl loading, process acceleration and frequency, workpiece fixturing and workpiece material.

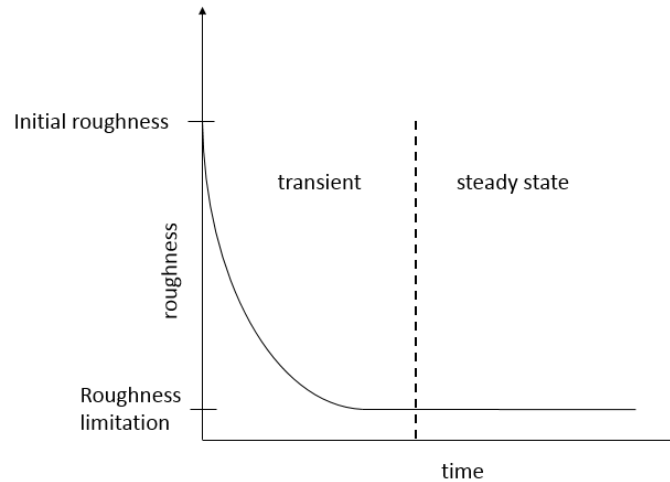


Figure 2.3 Basic rules of vibratory finishing as stated by Hashimoto [8], and graphed by [9]

2.6.1 Media type

Uhlmann et al. [10] investigated into the influence of abrasive media on surface topography formation of workpieces using steel rods ($\text{Ø } 40 \text{ mm}$) with different initial surface roughness values. It was observed that different media geometries (triangular or spherical) interact differently with the workpieces giving distinct material removal rates. Spherical media, for which the material removal mechanism relies mostly on abrasion and micro – cutting, it was stated that the relative velocity between the media and the workpiece is more important while in case of triangular media for which the material removal mechanism relies mostly on cutting the intensity of impact of media determines the material removal rate.

Wang et al. [11] experimentally investigated vibratory finishing of two aluminum alloys. The objective of this study was to correlate the changes in workpiece hardness and

surface roughness with the measured normal contact forces in a bowl-type vibratory finishing machine and one of the principal variables in this study was media size. The changes in workpiece hardness and roughness were characterized by varying the media size and experiments were performed with 7 mm, 9mm, and 11 mm spherical ceramic media. A force sensor was incorporated into the cylindrical workpiece that recorded only the surface-normal forces. The average impact force, average impulse, and maximum impact force were recorded for different media sizes. It was observed that the wear conditions were relatively uniform for all workpiece surfaces and the average impact forces and average impact duration remained relatively the same for all testing conditions. Thus, the differences in hardness (i.e. the difference in initial workpiece hardness and the hardness induced because of vibratory finishing) and roughness were due to the smaller scale differences in the impact contact conditions. The hardness increased with the finishing time and for a given finishing time and lubrication condition, larger media tended to produce slightly greater hardness.

2.6.2 Bowl loading, process frequency, and acceleration

Domblesky et al. [12] studied the effect of roll/feed motion (roll is the rotation of media about its own axis while feed is the circular motion of the media about the axis of the vibratory equipment) and bowl loading (i.e. the total weight of media within the bowl) on the media-workpiece flow characteristics and analyze how it affects the behavior of the vibratory finishing machine. Through experimentation it was determined that the effect of roll/feed weight (i.e. the eccentric weight that contributes to roll and feed motion of media) on the bowl acceleration is more dominant than the effect of bowl loading. The bowl acceleration increased as the roll/feed weight was increased. Further investigation revealed

that the total roll weight has a greater effect on the resultant acceleration. It was experimentally evaluated that the material removal rate was a function of bowl acceleration and workpiece hardness. Harder workpieces had significantly lower mass removal rates. It was observed that the material removal rate increased for higher bowl accelerations. Also, larger differences in density between media-workpiece resulted in higher material removal rates. This needs further investigation because according to this conclusion, plastic media that has much larger differences in media – workpiece density would result in higher material removal rates than ceramic media. Study of bowl acceleration on surface roughness revealed that the resultant bowl acceleration did not influence the surface roughness.

2.6.3 Workpiece fixturing

Since the present work involves vibratory finishing of fixed aluminum workpieces, investigations into some of the recent research efforts in this particular area were carried out. Reduced cycle time, consistent surface finishes, and elimination of part on part collisions are some of significant advantages of vibratory finishing with fixed workpieces [13]. Ahluwalia et al. [13] compared vibratory finishing of fixed components to freely floating ones with respect to changes in roughness parameter, Ra . The vibratory system used in this study was a trough system (i.e. open tub). In this study, they performed two sets of experiments in order to quantify the changes in Ra values. One, where the workpieces were thrown into the bulk of media flow (and were free to float) and the other in which the workpieces were secured on a holder that was immersed into the center of the vibratory finishing trough. Two observations were made from these set of experiments. In contrast to the freely floating workpieces, the fixed ones reached the roughness saturation

as described by [8] within the processing time of 150 minutes. This was attributed to the increased relative velocity and interaction between the workpiece and media. The *Ra* values of the fixed workpieces remained constant at around 0.1 μm while Ahluwalia et al. observed a high variability in the *Ra* value (with a decreasing trend) for the freely floating workpieces. An examination of whether the vibratory finishing with fixed workpieces follow the three principles or rules set forth by Hashimoto [8] was also carried out and it was observed that these rules hold true for this type of vibratory finishing as well.

Ahluwalia et al. [14] carried out a separate study relating to vibratory finishing of fixed workpieces. In contrast to [13], both the trough (open tub) and the fixture holding the workpiece were vibrating in [14]. They identified two types of workpiece fixturing methods: static, which are bolted on the vibratory setup; or dynamic, which are freely floating in the media. A novel polishing method named as double vibro-polishing was introduced where the container as well as the fixture were subjected to vibrations. Similar to the previous study by this group, a comparison was carried out between finishing of workpieces mechanically fixed on a conventional vibratory setup (where only the container vibrates) and finishing of fixed workpieces in a dual vibro-polisher (where both the fixture and the container are vibrating). It was observed that the workpieces attached to a vibrating fixture had a steeper drop in *Ra* values than the workpieces that were attached to a mechanical fixture. This observation was attributed to the fact that when both the fixture and the container are vibrated, the impact forces imparted by the media and the relative velocity between the media and the workpiece are higher which results in more aggressive mechanical working of the workpieces.

2.6.4 Workpiece material

The literature pertaining to the effect of workpiece material on the material removal rate was studied. Empirical investigations by J. Domblesky et al. [15] on vibratory finishing of brass, aluminum, and steel demonstrated that brass had the highest material removal rate, while aluminum had the lowest, and steel demonstrated an intermediate material removal rate. The ratio of material density to specific energy (i.e. specific energy is a fundamental quantity in metal cutting) for each of the workpiece material considered in the study was similar indicating that the material properties by itself would not account for the differences in the material removal rates for the three materials. Further investigations revealed that for the materials considered, the product of workpiece mass times workpiece velocity is more influential in controlling the material removal rates rather than material properties alone.

2.6.5 Material removal models

Domblesky et al. [15] developed a material removal model that takes into account bowl acceleration, workpiece mass, workpiece density, workpiece velocity, and specific energy. Equation 2.1 represents the material removal rate.

$$M.R.R. = \frac{K \times \rho \times m_w \times a \times v_w}{U} \quad (2.1)$$

Where, K is the cutting factor, i.e., a dimensionless number that takes into consideration the media packaging effects that depend upon the geometry and type of media used, ρ is the workpiece density, m_w is the workpiece mass, a is the bowl acceleration, v_w is the workpiece velocity, and U is the specific energy that is regarded as a fundamental quantity in metal cutting.

Although the model neglected the ploughing action of media (i.e. displacement of workpiece material from one location to the other), effect of adjacent media, and assumed that the media cutting action remains relatively same over time, the relationships between material removal and process variables predicted by the model had a good agreement with the experimental study. The results of the experimental study indicated that the material removal rate is directly proportional to the bowl acceleration, product of mass and velocity, and the abrasive cutting factor.

Hashimoto [8] proposed an empirical based equation that predicts the material removal and surface roughness for a given set of vibratory finishing conditions. Two types of material removal mechanisms were identified for the vibratory finishing process. One that is based on constant material removal and the other that is based on the change of surface roughness. The former represents the material removal that is obtained as the process reaches a steady state while the later represents the material removal during the transient period of vibratory finishing and which is more relevant to the manufacturing industry. Of note here is that the material removal is in terms of workpiece diameter and this restricts the model to predict the amount of material removed for a workpiece with cylindrical geometry. Equation 2.2 represents the material removal during the transient period of vibratory finishing.

$$S(t) = m \times t + 2 \times 4 \times (Ir - Dr) \left(1 - e^{-\frac{t}{T}}\right) \quad (2.2)$$

Where, m is the constant material removal rate obtained as the process reaches a steady state, t is the process time, Ir is the initial roughness, Dr is the roughness limitation, and T is the time constant of vibratory finishing process. These system parameters were measured from experimental results.

In a recent study by Hashimoto [16], an extension to the previous mathematical model was proposed and for the very first time fundamental parameters such as the equivalent chip thickness and specific cutting energy obtained through vibratory finishing process were revealed.

2.7 Research efforts based on surface finishes

Empirical investigations pertaining to changes in surface topographies of parts processed in a vibratory finishing process are presented in this section. Model developments by researchers to predict the change in surface roughness is also briefly discussed.

Azimi et al. [2] studied the media-workpiece contact modes and the resulting changes in workpiece topography. High-speed video taken at 500 frames per second of media flow past stationary stainless steel workpieces having a rectangular cross-section was used as an input to a flow measurement technique called as PIV in order to measure the time averaged media flow. The stainless steel workpieces were processed for a duration of 8.5 hours and were taken out at regular intervals for measuring the processed surface at multiple locations using a scanning white light interferometer (SWLI). Playback of the high-speed video gave substantial insights into the way media interacted with the workpiece surface and the SWLI measurements provided a measure how the media interaction affected the workpiece surface topography. Thus, a versatile technique that combines surface metrology and high-speed imaging was investigated in this study. Observations made from the study provided explanation for two distinct surface topographies obtained after finishing: highly pitted surface and an isotropic surface. Based on the observations, it was concluded that continuous media contact with the workpiece

resulted in an abrasive action desirable for higher material removal rates while an intermittent and impinging contact resulted in a highly pitted surface with little material removal.

Prakasam et al. [17] investigated the mechanism of surface evolution in the vibratory media finishing process by measuring the changes in surface profile with process time. The goal was to identify the cause of changes in surface that was subjected to vibratory finishing (i.e. change in surface due to material removal or indentation type ploughing). A single-fly cutter in a CNC milling machine was used to generate uniform structured surface (surface with uniform profile peaks and valleys). The surface profile was measured at different locations on the surface after every 20 minutes of vibratory finishing and the processing time was 180 minutes. The mean line of the initial profile that was used as a datum was retained by masking one-half of the surface with a tape and the other half was subjected to media action. As observed by Hashimoto [8], the R_a values saturated with process time. The peak heights in the measured profile data decreased with the process time and it was stated that this was either a result of material removal or subsequent displacement of material to the valleys. Observed changes in the valley depths in the measured profile data was stated as sign of plastic deformation.

Uhlmann et al. [18] developed a model to predict the roughness change after a given process time and is based on geometric changes in the roughness profile during the transient period of vibratory finishing. The model requires the initial roughness profile and the material removal rate, which has to be determined before vibratory processing. Based on these values the model predicts the development in surface roughness over time and

estimates the process time needed to achieve a desired roughness of a workpiece. The mean error in the prediction of surface roughness is around -0.7 % to +2.1 %.

2.8 Research efforts using diagnostic tools that provide insights into process mechanics

In this section, various research efforts that have used diagnostic tools such as high speed imaging camera, force sensors, and media flow measurement equipment to gain insights into the mechanics of material removal in vibratory finishing are briefly summarized. As both the force (which in turn gives the pressure) and velocity are expected to affect the material removals, most of the sensor based research efforts have focused on measuring these parameters.

2.8.1 Force sensors to measure impact loads and velocity

Yabuki et al. [19] conducted experiments using the same media, workpiece, and finisher as used in [11]. In this study a newly developed force sensor was used that recorded normal as well as tangential contact forces produced by the media. A small color camera was used to videotape the motion of the media. After subsequent playback of this video, three mode of media contact were identified: free impact, rolling of isolated media, and a single piece of media being stationary on the surface while the other media rolls over it. Scanning electron microscope images of craters on the workpiece surface substantiated the presence of the three distinct media contact modes. A plot of number of impacts per second against normal impact force for dry and water-wet conditions revealed that the dry impacts were greater in magnitude, and that there were more impact events in dry conditions. This can be attributed to the high energy transfer from wall to media due to higher coefficient of friction in case of dry condition as in contrast to water – wet conditions. Media sliding

phenomenon was observed in water-wet condition but was not present in case of dry condition.

Baghbanan et al. [20] used the same force sensor of Yabuki et al. [19] to measure the normal and tangential forces imparted by the media in a tub-type vibratory finishing machine that vibrates at a higher frequency and amplitude compared to a bowl-type machine. Similar to Wang et al. [11], these forces were correlated with the resulting changes in surface roughness and hardness with additional parameters such as mass loss and residual curvature of the aluminum workpieces. The number of impacts and the magnitude of impact forces recorded in the tub-type finisher were higher than the bowl-type machine used in [11], [19]. Similar to [19], the dry impacts were higher in magnitude as well as more in number for tub-type machine. An increase in the workpiece mass approximately 0.6 g/cm^2 was observed in case of dry finishing due to deposition of media debris on the workpiece surface. This was not the case for wet finishing as the media debris was washed away by the water. The residual curvature of the aluminum workpieces as a result of plastic deformation, and the hardness increased with finishing time. The surface roughness significantly increased to around $3 \text{ }\mu\text{m}$ from an initial value of $0.5 \text{ }\mu\text{m}$ in case of dry finishing due to deposition of media debris while for wet finishing the roughness value remained approximately $0.5 \text{ }\mu\text{m}$ even after 150 minutes of finishing.

Ciampini et al. [21] measured the surface-normal impact velocities in a tub type vibratory finisher for types of spherical media (porcelain and steel). This work is an extension of [11] and [19] where the effective impact velocity is evaluated from the measured force signal. The major difference in this work is that the force sensor was fixed to the tub wall as opposed to a freely floating one. The effective impact velocity was

evaluated using the relationship between maximum force and impact velocity obtained by dropping the media on sensor from a known height. Impact velocity was evaluated at four different locations in the tub and it was observed that the highest effective impact velocity was obtained when the sensor was placed closer to the tub walls. The media mass present inside the tub was also varied and it was seen that by lowering the media and thereby increasing the tub amplitude, the effective impact velocity increased giving rise to more aggressive finishing. In contrast to the work implemented by [11] and [19] where the use of impact force to characterize the conditions in vibratory finishing was dependent on the sensor or workpiece surface compliance, the present study uses impact velocities that are independent of workpiece size, shape, material, and the sensor to evaluate the energy imparted to generic workpieces.

2.8.2 High speed imaging camera and application of PIV system to vibratory finishing

Fleischhauer et al. [7] proposed a versatile technique called as Particle Image Velocimetry (PIV) for measuring the flow of media within the vibrating container at a surface level (i.e. two dimensional). This technique uses a high speed imaging camera to capture the media motion inside the vibratory bowl at 500 frames per second. For every test performed in this study, 5060 frames (corresponding to 10.12 seconds) were captured by the camera and processed in a PIV software to obtain the time-averaged media motion inside the bowl. It was observed that experimentally measured media flow consisted of a weak random component that had repeatable statistical properties which were sensitive to changes in process parameters and type of media used for finishing. Through this study, it was shown that on filtering this random velocity component an indicator of process conditions that is sensitive to the various process parameters could be obtained.

2.9 Research effort that treat granular media as a continuum fluid

Experiments and statistical mechanical modelling by [22] revealed that the granular media when subjected to low-amplitude vibration, share many essential dynamical properties known and predicted in molecular hydrodynamic dense gas and liquid systems. These findings demonstrate that under typical vibratory finishing conditions, the simple fixed viscosity Navier-Stokes equations, provides a rigorous model of the time-averaged media flow [22], [23].

S. Wan [24] introduced a framework based on granular flow dynamics, tribology, and computational fluid dynamics for analysis of mass finishing processes. From a tribology point of view it was stated that the underlying mechanism in material removal in vibratory finishing process is likely to be a combination of two and three body abrasive wear or even sliding wear mechanism. Using the wear law as stated in [25], S. Wan derived equation describing the surface roughness and stock removal for three dimensional freeform surfaces as follows:

$$S_a = (S_i - S_\infty) \times \left(e^{-\frac{k_T p_g v_s t}{H}} \right) + S_\infty \quad (2.3)$$

$$h = (S_i - S_\infty) \times \left(1 - e^{-\frac{k_T p_g v_s t}{H}} \right) + \frac{k_s p_g v_s}{H} t \quad (2.4)$$

Where, S_a is the areal surface roughness at a processing time, t ; S_i , the initial surface roughness; S_∞ , the limiting surface roughness; h , the stock removal; p_g , the granular pressure; v_s , the relative velocity between the media and the surface of the workpiece at an incremental area of interest; and both k_T and k_S are wear coefficients. S. Wan categorized various mass finishing processes into a specific granular flow dynamic regime. Of which

vibratory finishing along with centrifugal disk finishing was categorized within the fluid regime thus making it possible to apply continuum based continuity and momentum equations to solve for the media flow using a CFD software package. The results of this CFD analysis can be used in Equation 2.3 and Equation 2.4 to obtain the subsequent surface roughness and stock removal.

S. Wan in a separate study [26] investigated the effect of fixing workpieces within the media flow field contained in a typical vibratory finishing bowl. Cylindrical workpieces ($\text{\O} 50$ mm diameter and height) made of brass and steel (selected due to their considerable differences in hardness value) were finished in a bowl-type vibratory finishing machine. Of note here is that the workpieces were held stationary. A continuum based model was invoked and the workpiece geometry were given as input to ANSYS CFX v. 12 software package. The experimentally observed media flow field was visually compared to the flow field simulated by the CFD software and a good agreement between the two was observed.

2.10 Summary

Despite the advancements in the vibratory finishing process, the underlying mechanism of material removal still remains unanswered. The root cause of this fundamental problem is the randomized nature of vibratory finishing processes which makes the selection of process parameters very difficult to predict. Thus to date, the implementation of this process for finishing of workpieces is undertaken on a trial and error basis and largely depends on the expertise of the machine operator. Several analytical, empirical, and numerical models have been developed with regards to vibratory finishing process and their key findings are as described below:

The relative velocity between the media and the workpiece, the local media flow induced pressure, and the vibratory nature of the process determines the rate of material removal.

The material removal mechanism in vibratory finishing process is believed to be similar to two or three body abrasive wear mechanism.

Selection of media (i.e. size, shape, and quantity) and the compound plays a very crucial role with regards to the desired surface finish on workpieces.

The three types of contacts seen in vibratory finishing processes are: a) direct impact, b) rolling over the surface, and c) scenario where a single piece of media is held against the workpiece surface while other media rolls over it.

Normal forces and high velocity media impacts are believed to be the main causes of plastic deformation seen in vibratory finishing.

The frequency of vibration has a significant impact on the cycle time with increased frequency leading to shorter cycle time.

Fixturing of workpieces reduces the cycle time due to increased media-workpiece contact forces and relative velocity. This has led to advanced developments in vibratory finishing processes which is termed as drag finishing.

There is still a need to develop a fundamental, physics model which is capable of predicting the surface finish uniformity and material removal. The work presented in this thesis explores the potential to use the outputs from CFD models to better understand media workpiece interactions, and ultimately assist in predicting process outcomes.

3 CFD MODEL DESIGN AND COMPARISON TO EXPERIMENTAL CONDITIONS

The work undertaken in this project explores the potential of modelling the granular media as a fluid. A continuum mechanics based approach is used to model media flow around a stationary workpiece placed in a bowl-type vibratory finisher. While a full 3D model of the system is beyond the scope of this work, a simple 2D model will be used to determine the usefulness of this approach in understanding the process fundamentals. The following sections outline the 2D experimental media flow measurement inside a vibratory bowl and the subsequent approach taken to model this flow in a CFD environment. For the initial design and development of 2D CFD model, no workpieces are introduced to the vibrating media. The CFD predicted media velocity fields are compared to experimentally measured velocity fields.

3.1 Experimental flow measurement of vibrating media

3.1.1 Vibratory equipment and operating conditions

The vibratory finishing system (Raytech AV-75), see Figure 3.1 (a), consists of an annular polyurethane bowl with outer diameter of 0.6 m and a capacity of 0.02 m³. For initial testing, approximately 25.6 kg of ceramic media (Rösler RSG 10/10 S which is an angle-cut triangular shaped abrasive media having a critical length of 0.01 m, see Figure 3.1 (b)) was introduced to the bowl.

Compound consisting of water and FC KFL (3% volume) Rösler solution was supplied to the bowl using a Newport peristaltic pump at a rate of approximately 1.9 l/hr. The compound is not recirculated but is sufficient to keep the media wet during operating conditions. No workpieces were introduced to the media for initial testing. An unbalanced motor running at about 1750 rpm is used to generate the process vibrations. It should be noted that only one vibrational frequency is possible with the present equipment but the vibrating amplitude on the other hand can be altered by changing the unbalanced masses attached to the motor. 80/20® aluminum extrusions are used to construct a frame adjacent to the vibratory bowl, see Figure 3.1 (a). A Redlake camera (Motionextra HG-XR) is mounted on this frame and is used to capture the motion of vibrating media inside the bowl at 500 frames per seconds (fps). For acquiring sharper images, the imaged region is illuminated by a variable voltage halogen lamp (ARRI EB 400/575 D) as seen in Figure 3.1 a). A typical single image taken by the camera is depicted in Figure 3.1 (b).

3.1.2 Particle image velocimetry (PIV) to measure media flow

The images captured by high speed imaging camera are processed in Particle Image Velocimetry (PIV) software (Dantech™, version 3.41.38) to obtain the time-averaged media velocity magnitude and phase. Specific details about the application of PIV to measure media velocity field in vibratory finishing are given in [7] and a detailed background on PIV can be found in [27]. PIV generated velocity vector map for media flow is shown in Figure 3.2. Before evaluating the velocity vector map, the images are calibrated by placing a 6 inch ruler within the camera FOV (see Figure 3.3). By selecting two points ‘A’ and ‘B’ corresponding to 0” and 6” location on the ruler, the calibration length (i.e. 152.4 mm) is assigned to the camera FOV. Of note here is the PIV spatial

resolution, i.e. the linear distance between two nodes or grid points at which the velocity is evaluated. For the present study, this spatial resolution is approximately 3.5 mm.

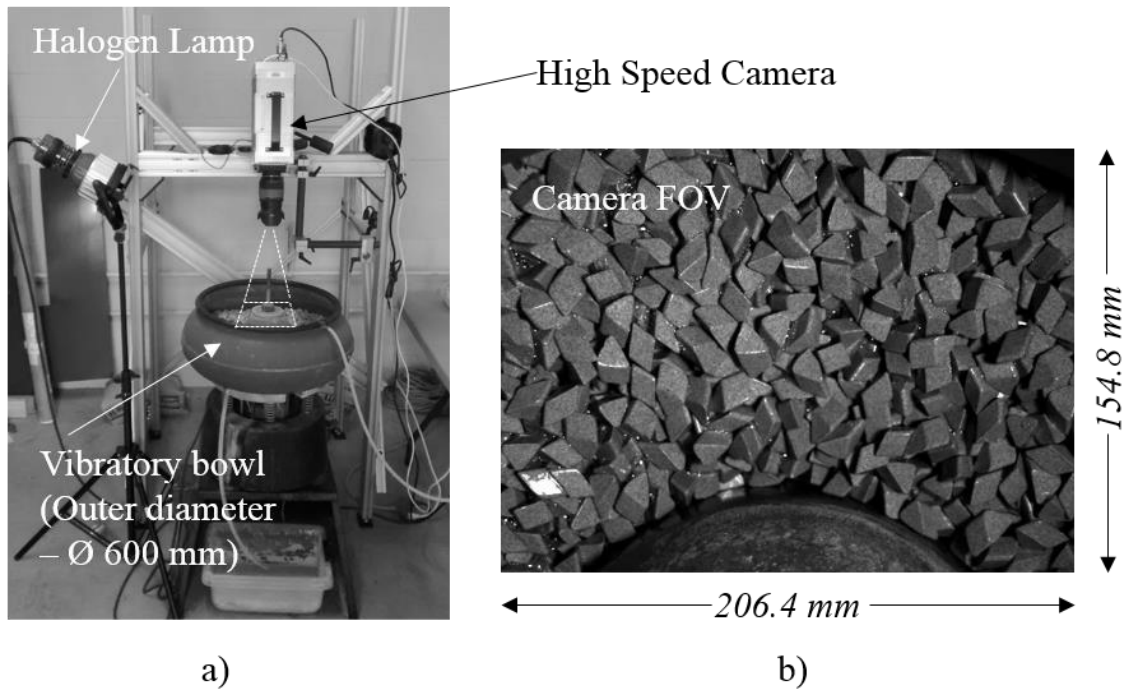


Figure 3.1 a) Experimental Setup, b) High Speed Camera FOV

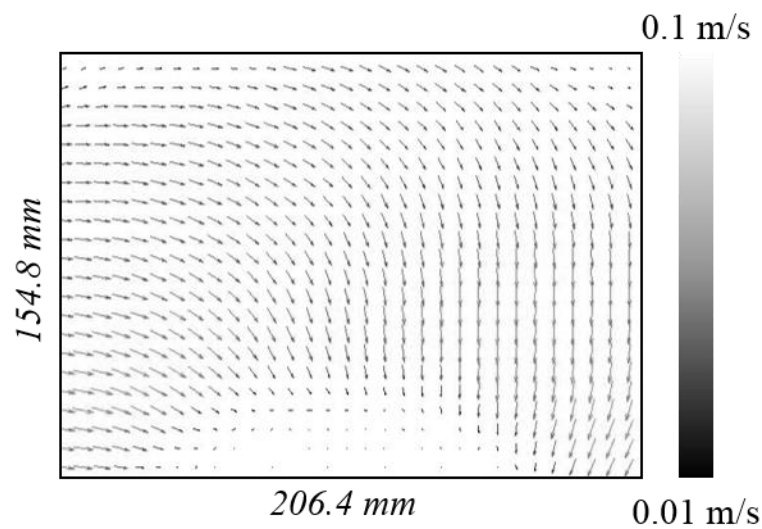


Figure 3.2 PIV generated velocity vector map of media flow

From Figure 3.2, it is observed that towards the center of the media flow field, media travels with a velocity in the order of 40 mm/s. A subsequent playback of the video made from high speed images of media motion helped to manually track the displacement of several individual media pieces over time. This simple check provided a useful verification of the PIV measured flow field and it was found that velocity magnitude observed by media tracking were similar to those measured by PIV. The vector map in Figure 3.2 will further provide input velocities to boundaries defined in CFD model and will later be compared to the CFD predicted media velocity field.



Figure 3.3 Image for calibrating the PIV velocity vector map

3.2 CFD model implementation

Any form of CFD is unconditionally based on the three fundamental physical principles governing all of the fluid flow dynamics: a) mass is conserved, b) Newton's second law ($F = ma$), and c) energy is conserved. Applying these principles to a model of the flow will result in equations that are a mathematical representation of a particular physical phenomenon involved [28]. The numerical solution of the model is obtained through solving these governing equations by subjecting them to physical boundary conditions. To model the flow of media in a CFD environment and in order to solve its

numerical solution, boundary conditions such as inlet velocities, density, and viscosity are obtained from experimental data and are discussed in details in the following sub-sections. A road map for modeling the flow of media and thereby implementing a CFD model of the flow that can provide insights into flow conditions is shown in Figure 3.4.

3.2.1 CFD software package

Student version of ANSYS® is used for the design and development of CFD model that delineates the media flow conditions at a surface level in the vibratory bowl. Particularly the ANSYS® FLUENT® module is used for the flow analysis and numerical evaluation of the flow outputs such as pressure and velocity distributions.

3.2.2 Control volume and mesh generation

In order to model the flow of granular media observed at surface level in a bowl type vibratory finishing machine within a CFD environment, it is important to clearly define the control volume i.e. the region of interest of media flow. The design modeler in ANSYS® is used to sketch the geometry of the control volume and create a planar surface body using the boundaries of the sketched geometry. A rectangular domain that is subset of the field of view of high speed imaging camera is chosen as the control volume for media flow analysis, see Figure 3.5 (a). Of note here is, the camera can record the media flow only in a horizontal plane. Thus, only 2D experimental data is available and the control volume in ANSYS® for numerical simulations is restricted to 2D.

Although the control volume is considered as a continuum, the solution of the governing equations of media flow is a function represented by finite number of points within this rectangular flow domain. This is a very common practice and the process of approximating the solution of a continuous problem by treating it as a discrete problem is

referred to as discretization. In modern CFD software packages, discretization is achieved via a technique called as mesh generation. The meshing module in ANSYS® is used to divide the control volume into a number of smaller subdomains made of triangular elements of side length ranging from ~ 2 mm to ~ 0.02 mm, see Figure 3.4 b. Calculations are performed over this discrete two dimensional mesh distributed across the control volume to obtain the numerical results.

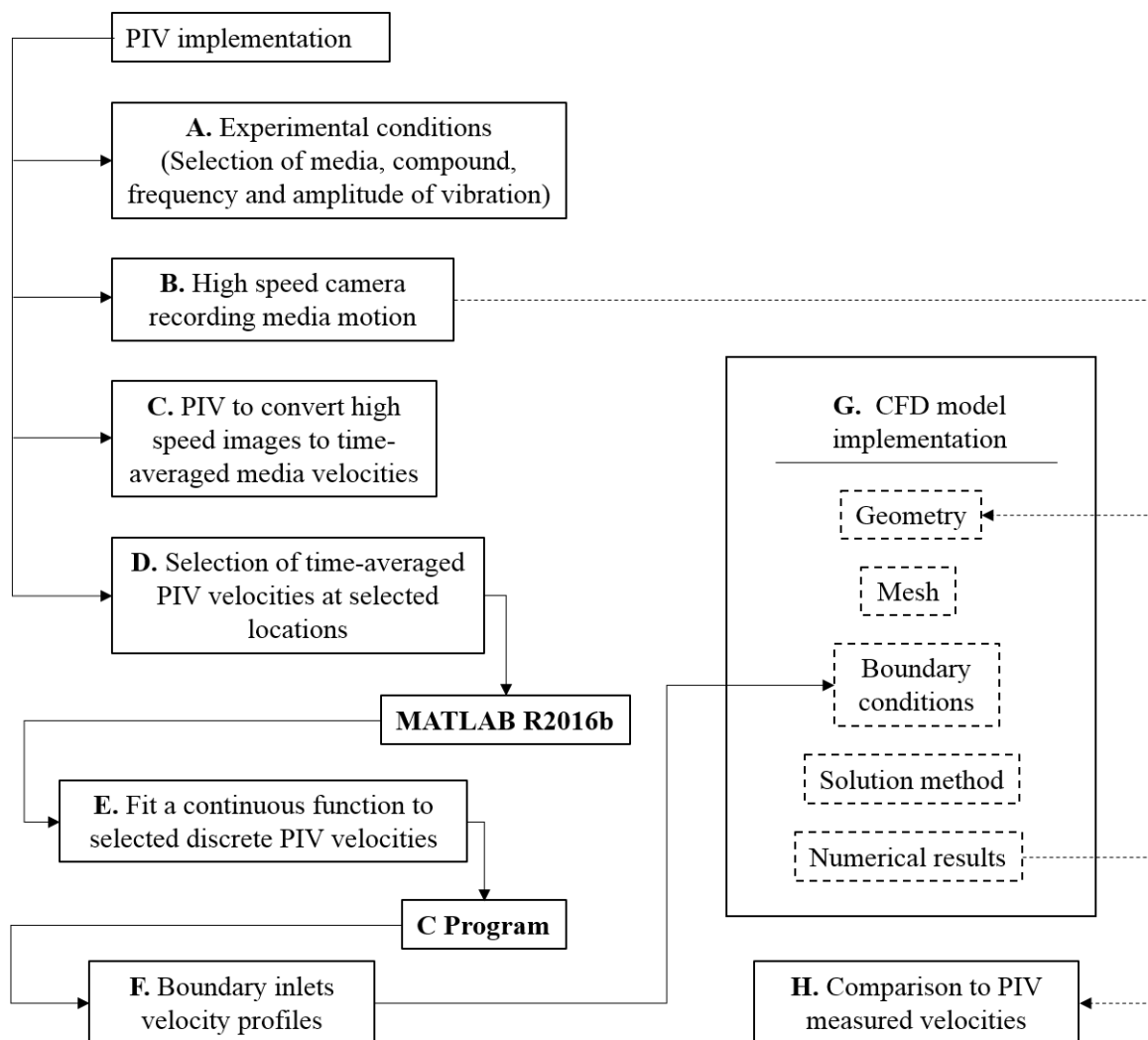


Figure 3.4 Road map for CFD model implementation

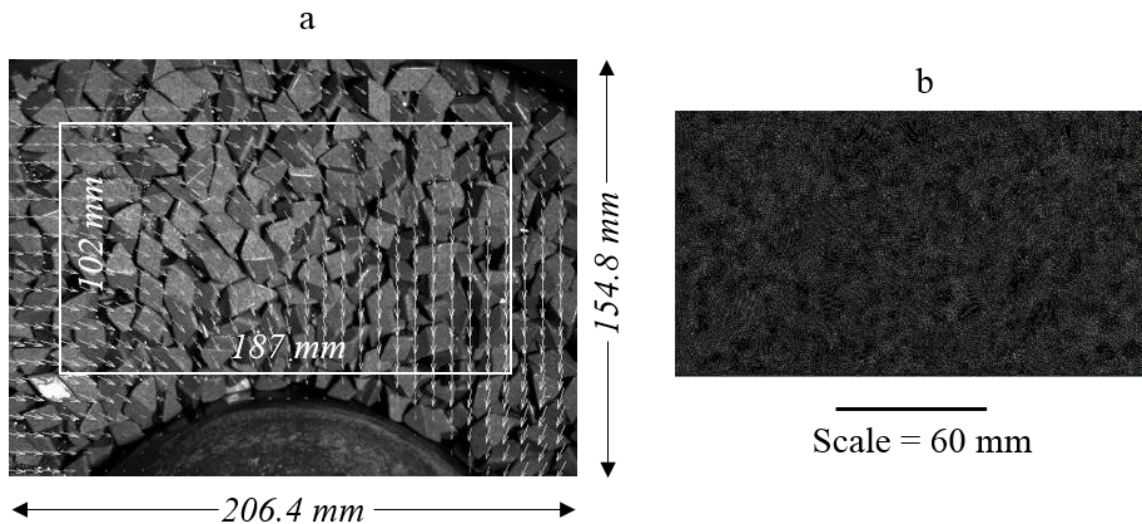


Figure 3.5 a) Control volume for CFD analysis and b) Meshing

3.3 Inputs to CFD model

3.3.1 Media density

The packing density of RSG 10/10 S media is experimentally determined by measuring the weight of media pieces packed in a container of known weight and volume. Of note here is the randomness in the packing of media within the container and the corresponding variations that it induces in the measured weight of the packed media. This weight is measured on an Ohaus scale (Navigator XT, 0.5 gram resolution). The packing density is evaluated by taking the ratio of weight of the packed media pieces to the volume of the container, see Table 3.1, and resulting density of 1535.33 kg/m^3 is obtained. In order to account for the randomness in the media packing, the media was packed in the container multiple times and each time its weight measured. This resulted in a variation of $\pm 200 \text{ kg/m}^3$ in the measured density of media. In a separate set of experiments, Dr. Tkacik measured the media packing density by suspending a plastic bag of media in a water tank

and by measuring the amount of water displaced. This resulted in a density value of 1390 kg/m³ that is comparable to the density obtained using the other method. The density in the model was set to 1390 kg/m³ since this value was used for determining the media viscosity.

Table 3.1 Media packing density

Media Type	Container weight (grams)	Container volume (litres)	Measured weight (grams)	Weight of packed media (grams)	Average weight of packed media (grams)	Packing Density (kg/m ³)
RSG 10/10 S	120	1.42	2280.5	2160.5	2180.17	1535.33
			2303.5	2183.5		
			2316.5	2196.5		

3.3.2 Dynamic viscosity

The dynamic media viscosity was experimentally evaluated by Eric Fleischhauer and Dr. Peter Tkacik. While a paper is being prepared on the topic, the following description gives an overview of how the viscosity was evaluated. For calculating the dynamic viscosity of media, the drag force exerted on a small cylinder (Ø 25.4 mm) by the media as it flows past it was measured using a very low range load cell. The empirical relation between drag force, $C_d = F_d / (0.5\rho V^2 A)$ and Reynolds number $Re = \rho V d / \mu$, is used for calculating the dynamic media viscosity [29]. Here F_d is the measured drag force, V is the PIV measured time-averaged media flow velocity past the cylinder, ρ is the media density, and A is the projected area of the cylinder. Thus the media viscosity for RSG 10/10 S is evaluated as 6.02 Pa.s and is set to this value in the CFD model. This media viscosity value is comparable to that of molasses which has a viscosity of 6 Pa.s. While undoubtedly there is uncertainty associated with the evaluated viscosity value, the CFD model is subjected to a sensitivity analysis where the model outputs are compared to a reasonable range of viscosity values in order to account for this uncertainty. This is later described in section 3.5.1.

3.3.3 Inlet boundary velocities

Many iterations of CFD model design led to the realization that in order for the CFD to best replicate that actual flow field, the media flow velocities at the boundary inlets in CFD model should match the experimentally measured PIV velocity values at the corresponding locations. The CFD control volume which is a subset of the camera field of view is assigned three velocity boundary inlets (Top, Left, and Right) and a pressure boundary outlet as seen in Figure 3.6 (a). The subsequent inlet velocity values at these boundaries are set to match the experimental data. Experimentally measured media velocities are extracted from the PIV processed raw data file using a script written in MATLAB® R2016b (see Appendix A).

MATLAB® R2016b curve fitting module is used to fit a periodic function consisting of finite sine terms to the discrete PIV measured velocity components along the top, left, and right edges of the control volume that correspond to the three inlet boundaries in CFD model, see Figure 3.6 (a). This function representing the velocity profiles along those three edges is given as an input to a C program (see Appendix B). The C program is compiled and interpreted inside ANSYS® and the velocity profiles are subsequently linked at the corresponding three edges of the control volume. The pressure outlet boundary is imposed with a pressure value equal to the ambient atmospheric pressure. Before diving into the evaluation of various CFD metrics, a simple sanity check to verify whether the experimentally measured velocities were successfully imposed on the boundaries of the CFD domain is necessary. Figure 3.7 shows a comparison between experimentally measured and computationally evaluated velocity components at the three inlet boundaries of the control volume and a reasonable agreement between the two is observed.

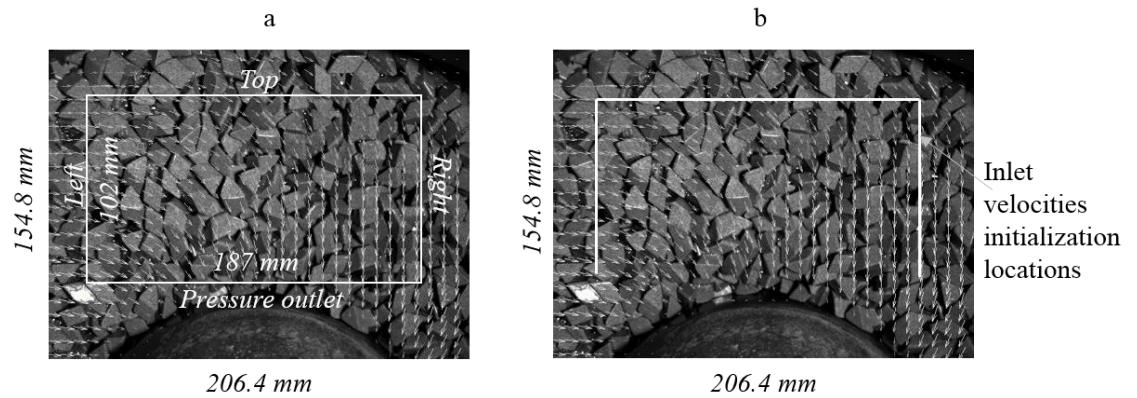


Figure 3.6 a) CFD inlet and outlet boundaries and b) solution initialization location

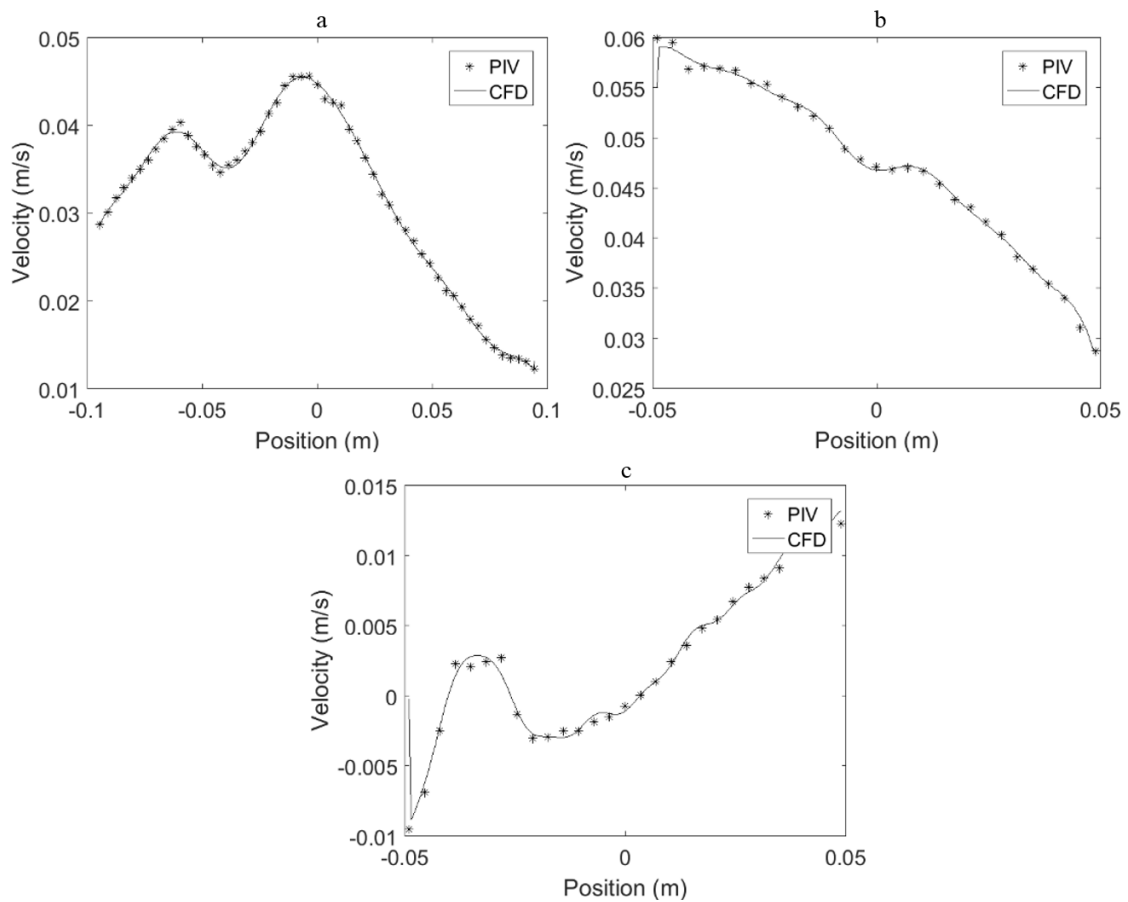


Figure 3.7 Experimental (PIV) and numerically evaluated (CFD) velocity component at a) Top edge, b) Left edge, and c) Right edge

3.3.4 Solution initialization and method

The CFD solver in ANSYS® Fluent® allows to specify initial values for flow variables such as gauge pressure, X, Y, and Z velocities either equal to value at a particular inlet boundary or equal to average value of all inlet boundaries. Selecting the former, the initial velocity values are set equal to the PIV measured values at the top inlet boundary (see Figure 3.6 (a)). SIMPLE (Semi Implicit Method for Pressure Linked Equations) algorithm details of which are outlined in [30] is used to solve the differential equations governing the media flow inside the control volume. The solution time is less than a minute.

3.4 Comparison between CFD and PIV velocity field

In order to validate the numerical solution of the CFD model, the CFD derived velocity field is quantitatively compared with the PIV measured velocity field using a script written in MATLAB® R2016b (see Appendix D) that calculates the percentage error in velocity magnitude and phase according to Equation 3.1 and Equation 3.2.

$$V_{err} = \frac{V_{PIV} - V_{CFD}}{V_{PIV}} \times 100 \quad (3.1)$$

$$\theta_{err} = \frac{\theta_{PIV} - \theta_{CFD}}{\theta_{PIV}} \times 100 \quad (3.2)$$

V_{PIV} , θ_{PIV} are experimentally (PIV) measured velocity magnitude and phase respectively whereas V_{CFD} , θ_{CFD} are CFD derived velocity magnitude and phase respectively. Mathematical correlations, $V = \sqrt{V_x^2 + V_y^2}$ and $\theta = \arctan\left(\frac{V_y}{V_x}\right)$, are used to calculate the velocity magnitudes and phase where V_x and V_y are the components of the velocity along the two coordinate axes. From Figure 3.8, it is observed that the CFD

predicted velocities exhibit the same range of magnitudes as those measured experimentally (PIV). Of note here is that the PIV and CFD velocity vector fields have different resolutions, i.e. the number of nodes or grid points at which the velocity is displayed is different for PIV and CFD with CFD having the greater number of nodes. The spatial resolution for PIV is approximately 3.5 mm between nodes while in the CFD the lateral distances ranges between 0.02 mm to 2 mm. This makes a direct comparison between the two data sets nontrivial. So in order to compare the CFD predicted and PIV measured velocity field, the spatial resolution between the velocity nodes for PIV and CFD is forced to be equal. This is achieved by interpolating the CFD predicted velocities at PIV node locations. A smoothing spline function is fitted to the CFD predicted velocities in MATLAB® R2016b and the corresponding predicted velocities are calculated at PIV node locations. Percentage difference in velocity magnitudes and phases between PIV and CFD is calculated as per Equation 3.1 and Equation 3.2 and a contour plot of this percentage difference is evaluated in MATLAB® R2016b and is shown in Figure 3.9. It is observed that, in approximately the center region of the contour plot where the workpiece will be placed the percentage error in velocity magnitude is in the range of 10% ~ 25%. In general, the CFD predicted velocities are slower than the PIV measured velocities and the maximum error is near the bottom end of the control volume.

3.5 CFD model sensitivity

The assigned values for input parameters associated with media flow analysis such as media viscosity and inlet media velocity are measured by thorough experimentation. Undoubtedly, there is uncertainty associated with these values and therefore it is important to note the effect of changes in these parameters on the predicted velocity field.

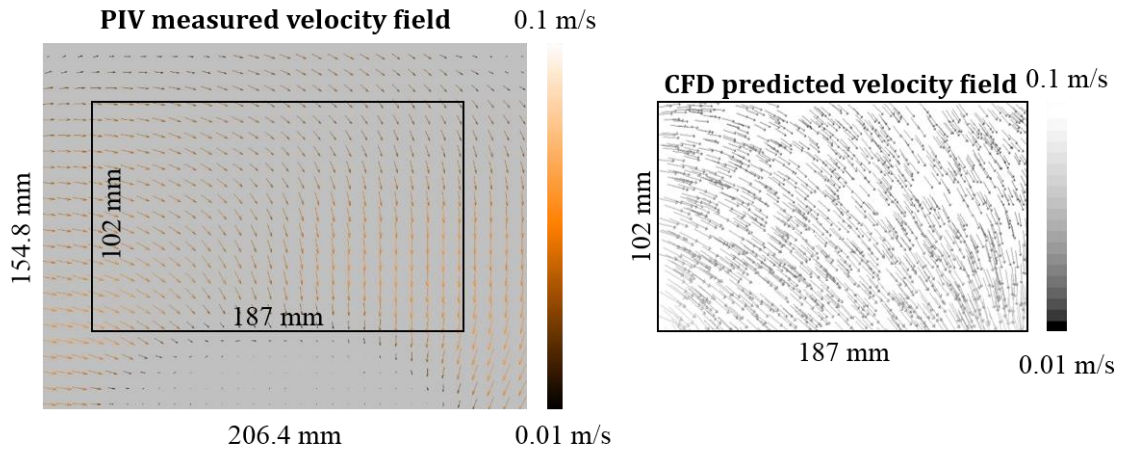


Figure 3.8 PIV measured and CFD predicted velocity fields

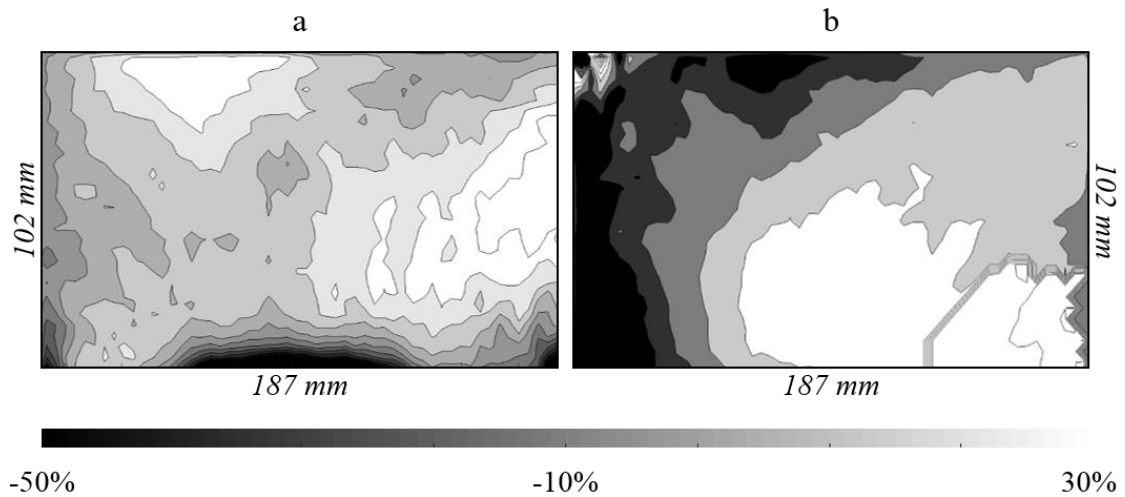


Figure 3.9 Percentage error in a) velocity magnitude and b) velocity phase

Furthermore there is a wide array of choices for selection of parameters like meshing scheme, algorithm for calculating the numerical solution, and initialization of flow variables. Optimal selection of these parameters depends upon the experience of the user and the requirements for modelling the flow. Thus the model is subjected to a sensitivity analysis with a goal to determine which parameters have a subtle or a significant impact on the predicted velocities and thereby provide an outline for selection of parameters best

suited for the application. The present model in which the media viscosity and density is set at 6.02 kg/m.s and 1390 kg/m³ respectively, and is discretized with triangular element mesh with side length ranging from 0.02 mm to 2 mm and which is initialized at top inlet boundary, is used as a reference model. Deviations in the resulting media velocity profile, due to altering any one of these input parameters, from the velocity profile obtained from reference model will help in determining the sensitivity of the model to that particular parameter. Following sub-sections discuss in detail about the influence of various input parameters on the predicted velocity fields. Velocity profile along a vertical line passing through the center of the control volume, see Figure 3.10 for location of vertical line, and velocity contours across the entire control volume are used to compare the effect of changing input parameters on model.

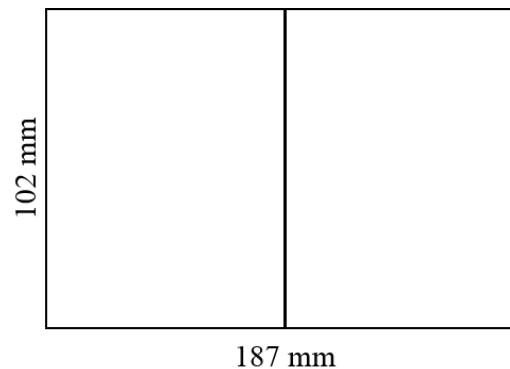


Figure 3.10 Location of vertical line within the CFD control volume along which the velocity profile is evaluated for comparing changes in input parameters

3.5.1 CFD model sensitivity to dynamic viscosity

Model in which the dynamic viscosity of media is set at 6.02 Pa.s is used as a reference model. As discussed in section 3.3.2, this viscosity value is experimentally evaluated and has some uncertainty associated with it. This uncertainty can in turn be attributed to uncertainty in various variables such as PIV measured velocity, Reynolds

number, media density, and drag force that are used in the calculation of viscosity value. Evaluating uncertainty in Reynolds number, measured PIV velocities, and drag force is extremely difficult and non-trivial. Hence for simplification, only the uncertainty in media density is taken into account. The resulting variation in media viscosity is found to be ± 0.05 Pa.s. The values for viscosity defined in the CFD model are varied as shown in Figure 3.11 and Figure 3.12 while the density is set at 1390 kg/m^3 and is kept constant throughout. Figure 3.11 is a contour plot of velocity magnitude across the control volume for given range of viscosities while Figure 3.12 graphs velocity profiles for given range of viscosities along a vertical line as indicated in Figure 3.10. As a frame of reference, the various viscosity values defined in the model can be compared to some of the common fluids such as water ($\mu = 0.00089$ Pa.s), blood ($\mu = 0.003$ Pa.s), glycerin ($\mu = 0.95$ Pa.s), honey ($\mu = 2$ Pa.s), chocolate syrup ($\mu = 10$ Pa.s), and ketchup ($\mu = 50$ Pa.s). From Figure 3.11 and Figure 3.12, it is observed that orders of magnitude changes in viscosity are required to noticeably affect the predicted velocity fields.

3.5.2 Model sensitivity to meshing style

Effect of meshing style, i.e. the shape of the 2D mesh elements, on model output is evaluated. Figure 3.13 shows a comparison between velocity profiles obtained for triangular and quadrilateral mesh elements, both having a side length that ranges between 0.02 mm to 2 mm. It is observed that there is no noticeable change in the velocity profiles for both mesh elements. Same observation can be made from the Figure 3.14 that maps the velocity distribution across the entire control volume for triangular and quadrilateral mesh elements.

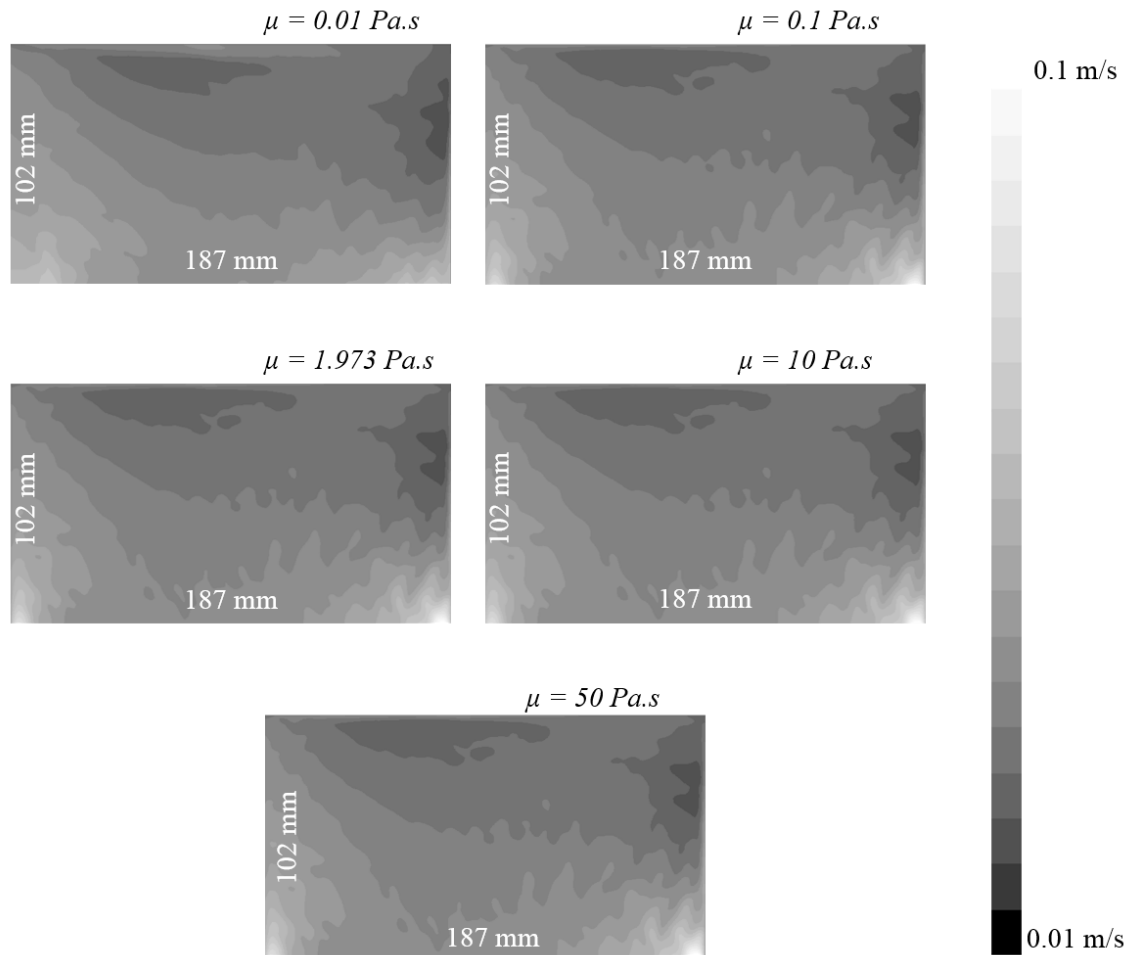


Figure 3.11 Velocity distribution across the entire control volume for a range of dynamic viscosities

3.5.3 Model sensitivity to meshing density

Accuracy of the model mainly depends on the level of meshing of the fluid domain, i.e. spacing between the grid points where large gradients in flow-field properties exist [28]. This spacing should be adequate enough so that it can capture at least some of the real aspects of flow. A comparison between the computed velocity distributions across entire control volume and velocity profiles for coarse and fine meshing density are shown in Figure 3.15 and Figure 3.16 respectively.

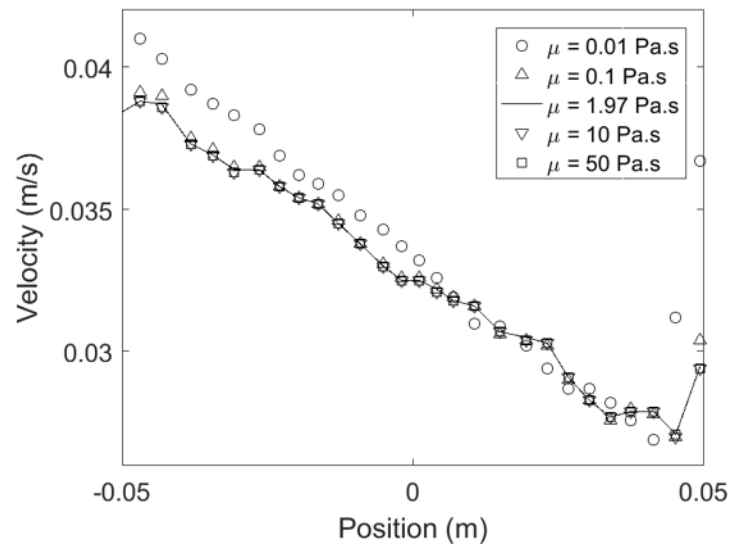


Figure 3.12 Velocity profiles for a range of dynamic viscosities

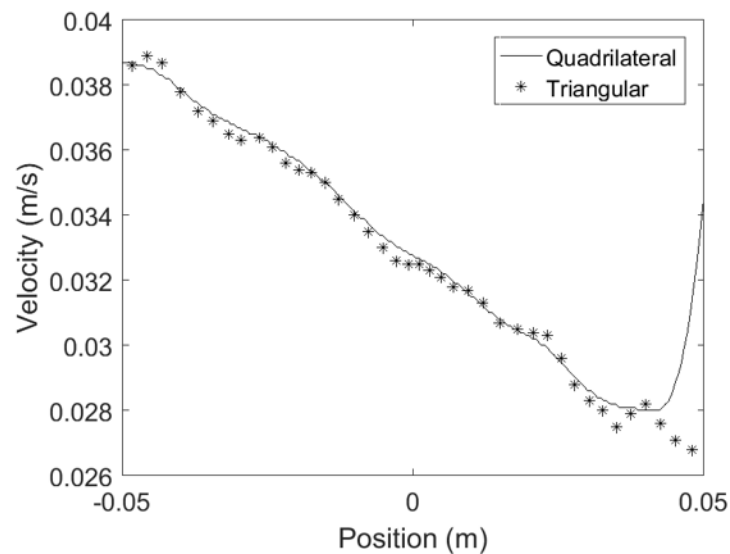


Figure 3.13 Velocity profile for different meshing styles

The control volume that is discretized with a coarse mesh has total 900 elements and the side length of the elements is approximately 6 mm whereas the control volume that is discretized with a finer mesh has total 1,42,304 elements with side length of elements ranging between 0.02 mm to 2 mm. Of note here is the difference in the computation time for the CFD solver to compute the solution of governing equations of media flow. For a

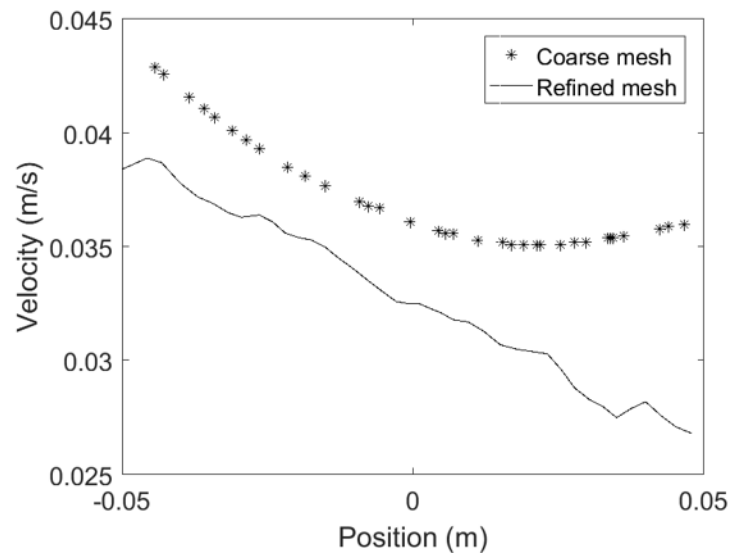


Figure 3.16 Velocity profile for coarse and refined mesh

It is observed that the velocity distributions are clearly sensitive to meshing density. It can be seen that even though the values exhibit similar trend in the profiles and contours there is a variation in the magnitude of these values. This suggests that with a finer mesh more details of media flow are captured which is not the case for a coarse mesh. One way to evaluate the required density of mesh is to compare the numerical results with the experimental data. This will not only improve the numerical accuracy of the CFD calculations but also minimize the computational time.

3.5.4 Model sensitivity to initialization of flow variables

Initialization of flow variables, i.e. assignment of initial value for a given flow parameter, can be carried out at a particular boundary or an average value based on all the boundaries may be used for the initialization. A straightforward comparison between the velocity fields across the control volume obtained from a model initialized at the three boundaries (top, left, and right) separately and that measured experimentally yielded smaller percentage differences for the model that was initialized at the top inlet boundary.

Thus, in the present study, the model is initialized at the top inlet boundary. Another justification for this is the nature of media flow within the vibratory bowl. The media flow field is toroidal, where the media flows from the outer edge of the bowl towards the center of the bowl. Figure 3.17 shows the velocity profiles along a vertical line (as indicated in Figure 3.10) for different initialization boundaries. It is observed that the model is strongly sensitive to boundary at which the flow variables such as velocity, density, and viscosity are initialized. Same observation can be made from Figure 3.18 that maps the velocity distribution across the control volume for different locations of flow variable initialization.

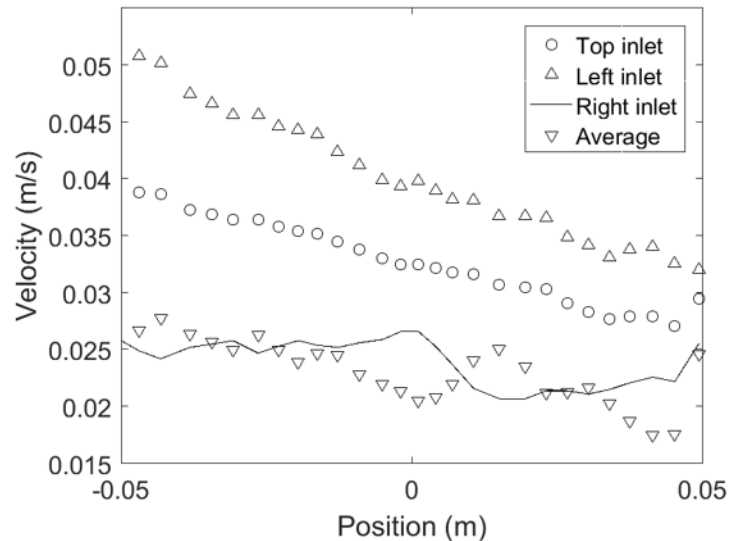


Figure 3.17 Velocity profiles for different locations of flow variable initialization

3.6 Synopsis of CFD model sensitivity analysis

The above observations are briefly summarized in Table 3.2. The parameters to which the predicted velocity fields are highly sensitive to are the meshing density and the initialization boundary of flow variables.

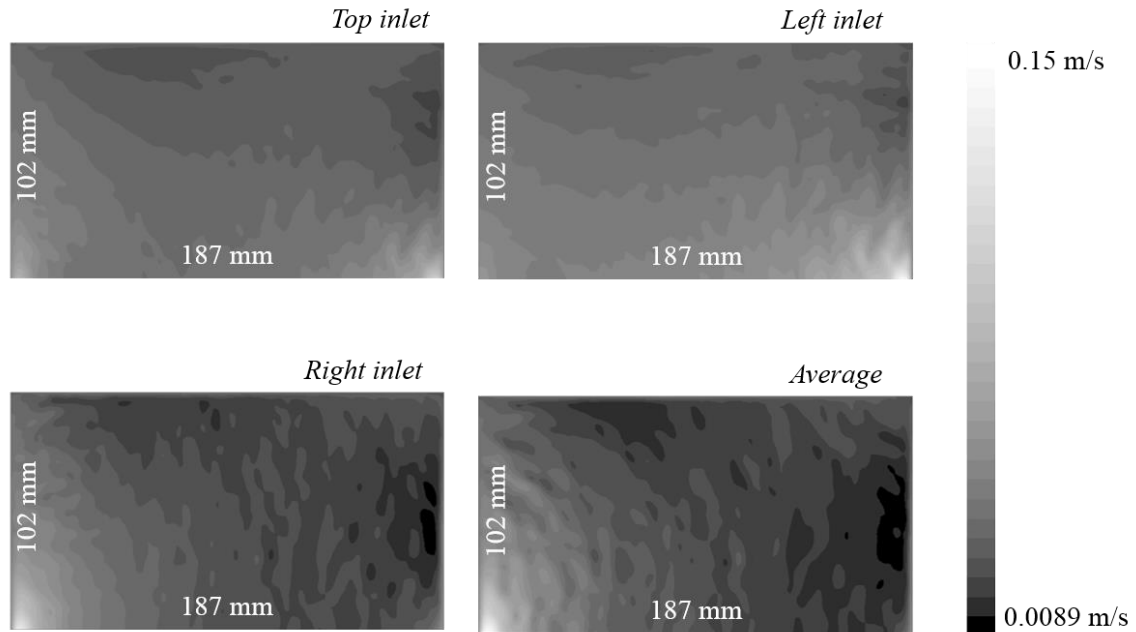


Figure 3.18 Velocity distribution for different locations of flow variable initialization

Table 3.2 Parameter sensitivity to model outputs

Parameter	Type	Effect
Meshing density	Coarse mesh (element size: Approx. 6 mm)	Highly sensitive. Mesh density dictates the numerical accuracy.
	Refined mesh (element size: 0.02 - 2 mm)	
Meshing scheme	Triangular mesh elements (side length: 0.02 - 2 mm)	Not sensitive. No noticeable change in predicted velocity fields.
	Quadrilateral mesh elements (side length: 0.02 - 2 mm)	
Fluid properties	Density (1000, 1535.33, 2000, 2500 kg/m ³)	Not sensitive for a given range of values. Orders of magnitude change is required to noticeably affect the velocities.
	Viscosity (0.01, 0.1, 1.97, 10, 50 Pa.s)	
Initialization boundary for flow	Top inlet	Highly sensitive. Accuracy of the predicted flow field depends on initialization boundary.
	Left inlet	
	Right inlet	

3.7 Summary

A rigorous methodology to implement a two-dimensional CFD model that depicts the media flow at a surface level inside a bowl-type vibratory finishing machine is outlined in this chapter. The input boundary conditions to the model were obtained experimentally by measuring the media flow properties (i.e. density and viscosity) and the subsequent

media flow field. A novel application of PIV to a vibratory finishing process is implemented to measure the two-dimensional media flow field. Despite the uncertainty in the measurement of media flow properties and the flow field (i.e. viscosity, density, and velocity), the outputs of the CFD model have a reasonable agreement with the experimental data. The percentage difference between the PIV and CFD velocity magnitudes is approximately 5 % near the three boundary inlets and it increases to 25 % towards the bottom edge of the computational domain. In general, the CFD predicted velocities are slower than experimentally measured media velocities. Nevertheless, initial observations shows the significant potential of the modelling approach and provides further supporting evidence that the media can be treated as a fluid. In the following chapter, the CFD model is extended further to predict the media flow around a stationary workpiece in order to gain insights into the process outcomes.

4 EXPERIMENTAL TESTING: SURFACE TOPOGRAPHY VARIATIONS RESULTING FROM MEDIA APPROACH ANGLES

As previously mentioned, the central goal of this work is to develop a numerical model of media flow around stationary workpiece in a CFD environment that can provide insights into surface finish and resulting surface topography of workpiece due to different media flow conditions observed in a bowl – type vibratory finishing machine. In order to materialize this goal, experimental investigation is carried out on two identical workpieces, each subjected to a different media flow condition. The chosen flow conditions are selected to gain insights when the workpiece is tangential to and normal to the time averaged media flow direction.

4.1 Experimental setup

The vibratory finishing system as described in section 3.1.1 and shown in Figure 4.1 was used for finishing of two precision ground aluminum 6061 T6 workpieces. Approximately 25.6 kg of Rösler ceramic media (triangular shaped angle – cut media having a critical length of 10 mm) was placed in the bowl and Rösler compound (solution prepared by mixing water and 3% FC KFL) was supplied at 1.9 l/hour to keep the media wet during finishing. Vibratory system specifications and implementation of PIV to measure time – averaged media flow around the workpiece, as described in section 3.1.1 and 3.1.2, were repeated.

4.2 Workpieces

Precision ground aluminum 6061 T6 stock having a rectangular cross – section with a material density of 2700 kg/m^3 and ultimate tensile strength around 330 MPa is selected for the experimental study. The primary reason for selection of this workpiece material is because of its lower hardness value that makes it more susceptible to higher processing rates and thereby minimizing the experimental time required in the experiments.

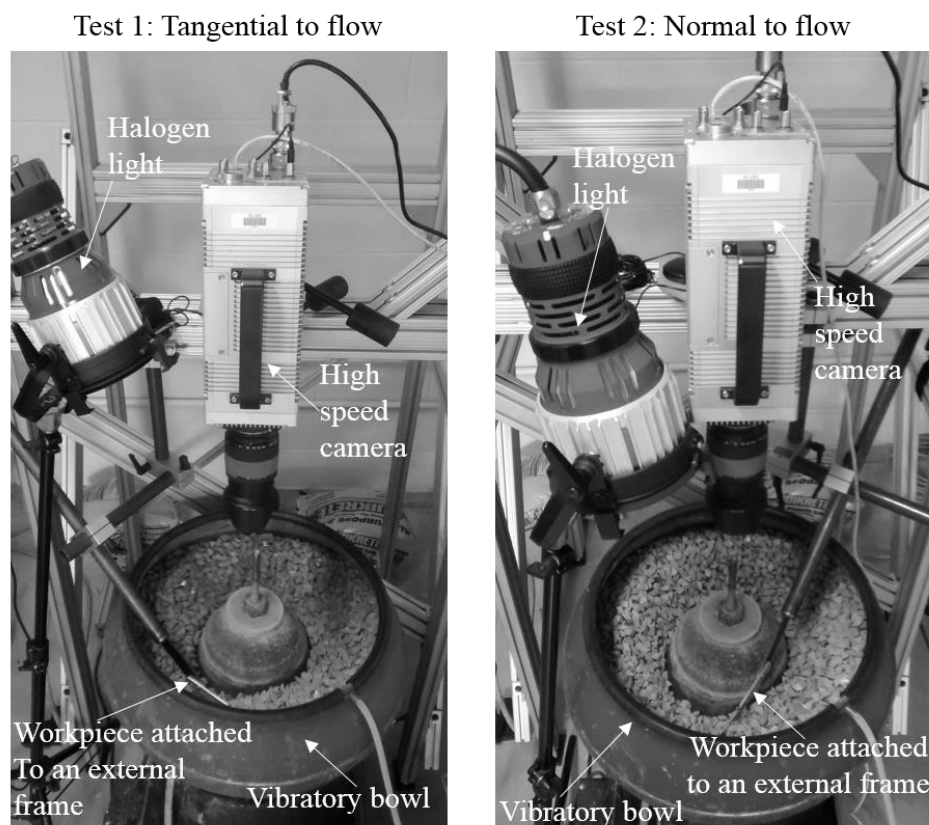


Figure 4.1 Experimental setup. (Left) Tangential near – workpiece flow. (Right) Normally – impinging near – workpiece flow

Precision ground stock was selected to reduce the workpiece form variations/waviness error. Prior to finishing in the vibratory bowl, the workpieces were subjected to elementary machining operations. Based on the volumetric capacity of the

bowl, the workpieces were sawed and milled to dimensions (100mm × 50mm × 3mm) suitable for effective finishing in the bowl. As seen in Figure 4.2, an aluminum plate approximately 75 mm long and 20 mm wide is welded to the workpiece so that the workpiece can be mounted on a moveable fixture, made from three cylindrical arms, that provides the six degrees of freedom. This fixture is attached to the external frame, isolating the workpiece from bowl vibrations, and enable correct placement within the media flow, i.e. tangential or normal to the media. Additional features such as grooves (approximately 100 μm deep and 2 mm wide) and fiducials (approximately 50 μm deep and 0.56 mm in diameter) were milled on to the workpiece surface as shown in Figure 4.2. The purpose of the grooves and the fiducials is for a related study (evaluation of material removal uniformity) which is outside the scope of the present work. Though in the present work, the location of fiducials along with other markers such as sample number (which is inscribed on the workpiece) and the location of the weld region (see Figure 4.2) help in identifying the surface locations (i.e. left, right, upstream, downstream) used for the white light interferometer measurements (detailed in section 4.7).

4.3 Testing conditions

In each of the two different tests (tangential and normal to the media flow), the workpiece was held stationary within the vibrating media (see Figure 4.3). The chosen test configurations are selected to investigate the cases of tangential near – workpiece flow and normally – impinging near – workpiece flow. In each test, workpiece was processed in the vibratory bowl for a duration of 90 minutes. Similarly in each test, the media motion was recorded at 500 Hz for 10.12 seconds (corresponding to 5060 frames) by the high speed

camera. These frames were subsequently processed by the PIV software, details of which are provided in section 3.1.2.

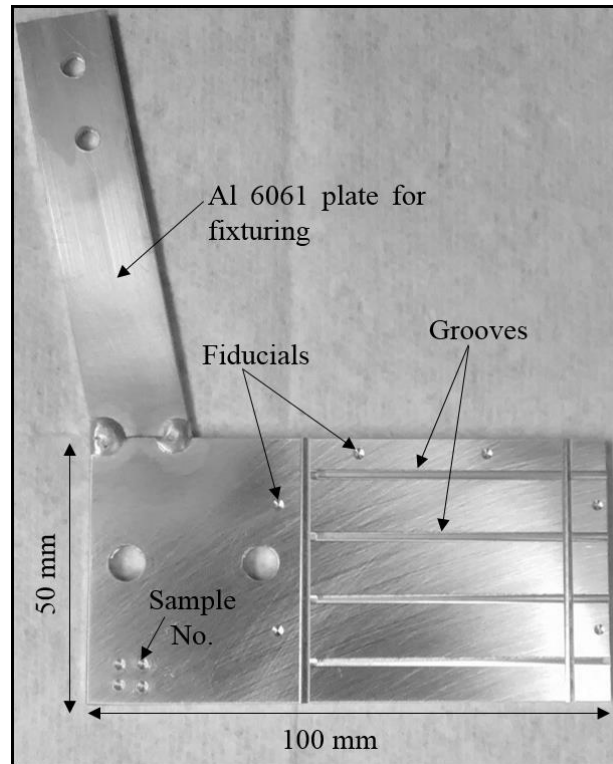


Figure 4.2 Ground aluminum workpiece

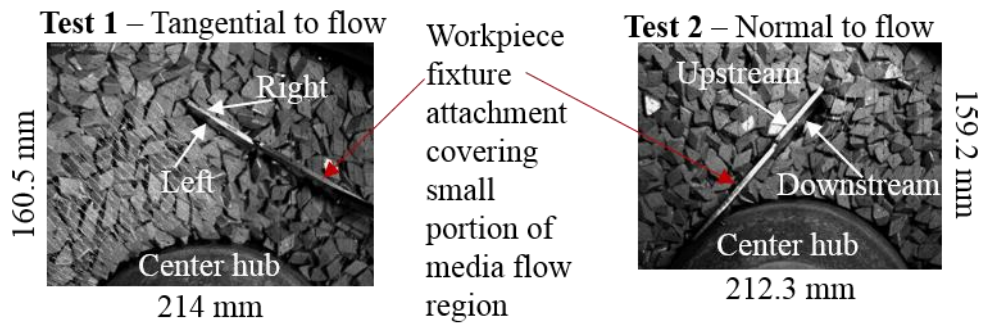


Figure 4.3 Testing conditions. (Left) Tangential near – workpiece flow. (Right) Normally – impinging near – workpiece flow

4.4 PIV results and inputs to CFD model of media flow around the workpiece

The PIV measured media velocity fields for Test 1 (tangential near – workpiece flow) and Test 2 (normally – impinging near – workpiece flow) are shown in Figure 4.4.

Of note here is, due to the presence of the center hub and the workpiece fixture attachment, a small portion of the media flow region as seen in the camera FoV is concealed (see Figure 4.3) and thus the PIV media velocity evaluation is near – zero in this region (see Figure 4.4). The outer dimensions (214 mm × 160.5 mm for Test 1 and 212.3 mm × 159.5 mm for Test 2) in Figure 4.4 correspond to the field of view (FoV) of the high speed imaging camera while the inner dimensions (189 mm × 98 mm for Test 1 and 189 mm × 91 mm for Test 2) correspond to the dimensions of the control volume defined in ANSYS® for CFD model that delineates Test 1 and Test 2 flow conditions. The selection of the size of the control volume is limited by the bowl geometry. Typically the control volume is selected such that it captures the essence of media flow field existing around the stationary workpiece. The boundary conditions for the two CFD models are obtained by repeating the procedure as described in section 3.3.

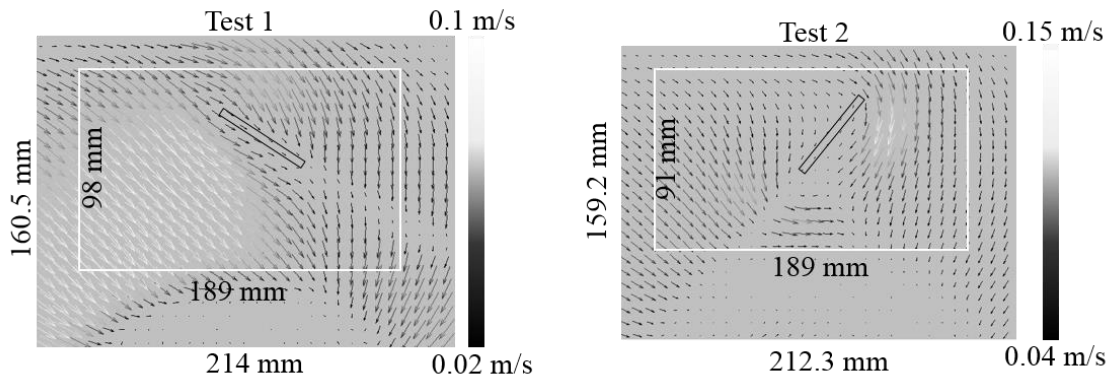


Figure 4.4 Time - averaged media velocity field evaluated using PIV for (Left) Test 1- tangential flow and (Right) Test 2 – normal flow as depicted in Figure 4.3

4.5 Comparison of CFD predicted media velocity field with PIV measured velocity field

Figure 4.5 (a) and Figure 4.6 (a) depicts the PIV measured velocity field for the two tests, while Figure 4.5 (b) and Figure 4.6 (b) depicts the media velocity fields predicted by the two CFD models. To validate the numerical solutions of these models, the CFD

predicted velocities are visually compared with PIV measured velocities for tangential and normal flow around stationary workpiece.

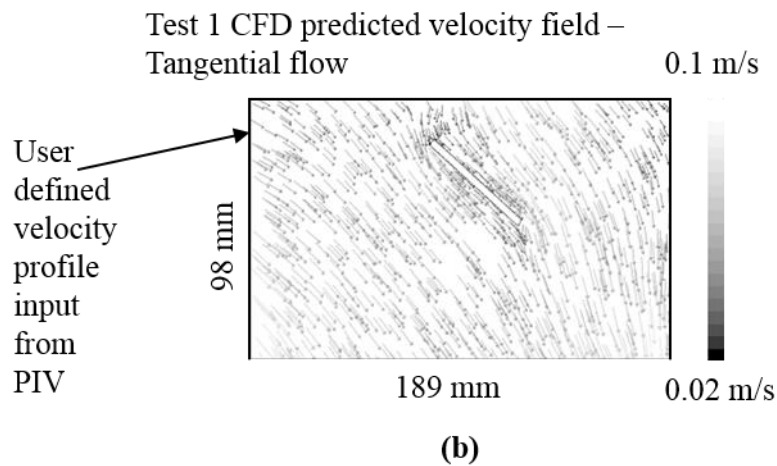
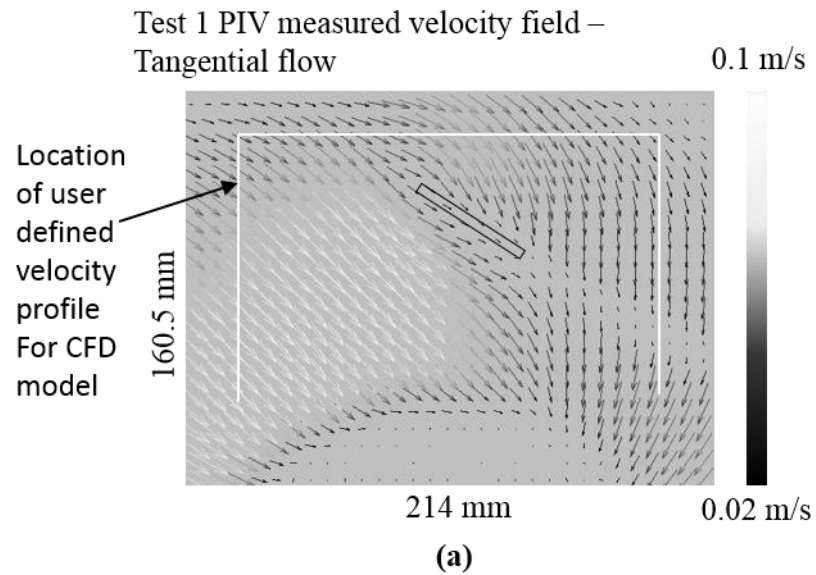


Figure 4.5 Comparison between PIV measured and CFD predicted velocity fields for Test 1 tangential flow

This initial visual comparison, reveals that there is reasonable agreement between the velocity magnitudes and flow structures. Experimentally measured and CFD predicted velocity profiles approximately 5 mm from workpiece surface are compared in order to further test the proposed modelling approach.

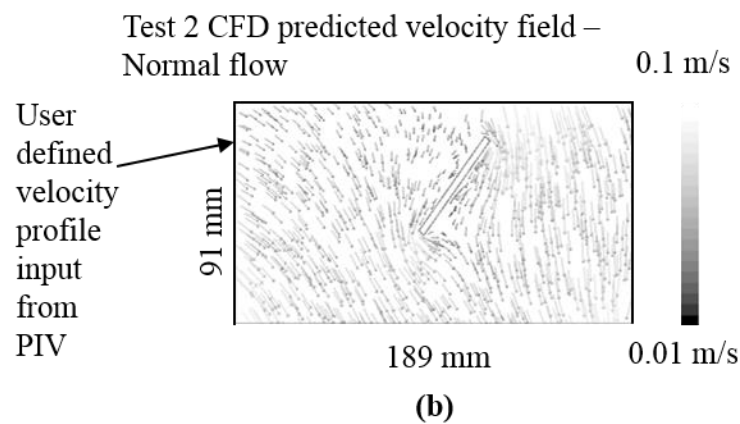
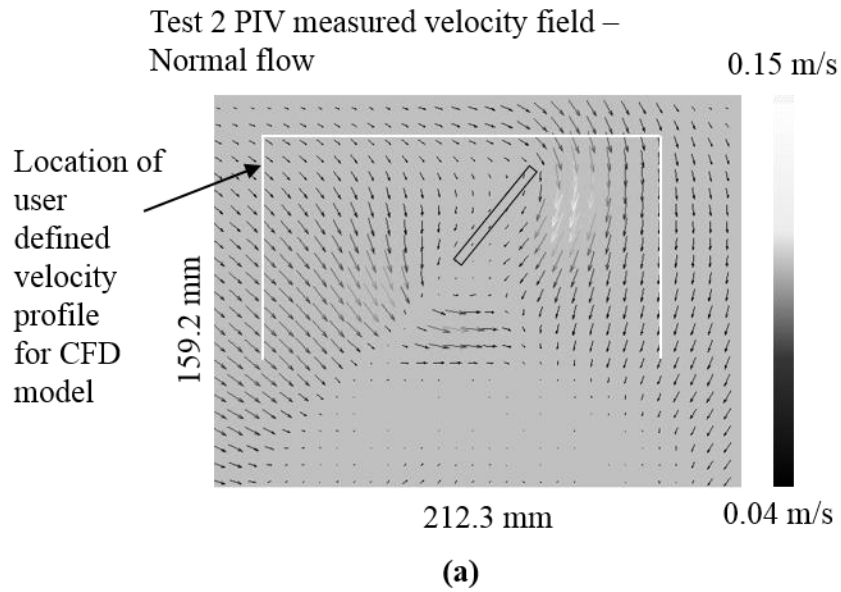


Figure 4.6 Comparison between PIV measured and CFD predicted velocity fields for Test 2 normal flow

A comparison between the CFD predicted and PIV measured tangential velocity profiles approximately 5 mm from workpiece surfaces (i.e. Left, Right, Upstream, and Downstream) is implemented to validate the accuracy of the CFD predicted flow model, see Figure 4.7. From Figure 4.7 it is observed that the measured and the computed velocity profiles exhibit similar flow structures for both tangential (Test 1) and normal (Test 2) media flow conditions. Though a slight difference in flow pattern is observed in case of Test 1 Right, the computed velocity magnitudes exhibit the same range of values as those

measured experimentally. This difference can mainly be attributed to the fact that the measured flow contains a significant normal (into-the-plate) component, which is not captured in the predicted flow (see Figure 4.5). This validation of CFD predicted velocity profiles with the measured velocity profiles supports the use of CFD modeling approaches and will be further explored in Chapter 5.

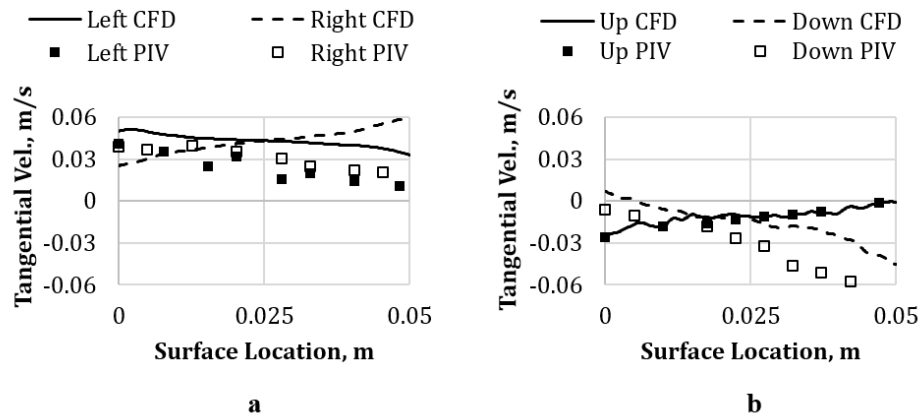


Figure 4.7 CFD predicted and PIV measured velocities: (a) Test 1, and (b) Test 2

4.6 Material removal

Though a separate study (which is outside the scope of present work) to evaluate the material removal uniformity obtained under the different conditions is underway, preliminary analysis of material removal was done by measuring the amount of mass loss in the two aluminum workpieces. The mass loss was measured on an Ohaus weighing scale (Adventurer Pro AV264C, 0.1 mg resolution (see Figure 4.8)) and was 44 mg and 21 mg for Test 1 and Test 2 respectively, see Table 4.1. This indicates that very little material was removed during finishing and that for the given workpiece – media combination, surface conditioning was more prevalent. If for the measured mass loss, the material removal is assumed to be uniform over the surfaces of the workpiece submerged in media, then the average reduction in height evaluated for the two workpiece surfaces (i.e. ‘Left’ and ‘Right’

for Test 1, ‘Upstream’ and ‘Downstream’ for Test 2) was 1.92 μm and 1.01 μm for Test 1 and Test 2 respectively, as given in Table 4.1 (average height reduction values are divided by two since uniform material removal is assumed on the two workpiece surfaces).

Table 4.1 Mass loss evaluation for analyzing material removal

Flow condition	Average Mass loss (grams)	Average submersion length (mm)	Width (mm)	Material Density (g/mm^3)	Average Height Reduction/surface (μm)
<i>Test 1 Tangential flow</i>	0.0438 (± 0.0007)	82.82	50.85	0.00271	1.92
<i>Test 2 Normal flow</i>	0.0213 (± 0.0006)	76.97	50.85	0.00271	1.01



Figure 4.8 Weighing scale to measure the amount of mass loss

4.7 Quantification of surface finishes

Evaluation of surface finishes is implemented using a Zygo ZeGage scanning white light interferometer (SWLI). Areal measurements were taken at 30 locations on each side of each of the workpiece pre- and post-finishing, see Figure 4.9. Each measurement was processed in MATLAB® R2016b (see Appendix C) and Zygo ZeGage Mx software (piston and tilt removed, 0.8 mm high pass filter) and two surface parameters were

calculated; Sq , and Str according to definitions given in [31]. Root mean square roughness (Sq) was included as it quantifies the rough nature of a surface. A surface with larger Sq value is indicative of its rough nature but as this Sq value decreases it indicates that a surface is getting smoother. The texture aspect ratio term (Str) was included as it quantifies the anisotropic nature of a surface. For example, a low Str value (closer to 0) indicates the presence of surface directionality, while a fully isotropic surface, as expected after successful vibratory finishing, will have a value closer to 1.

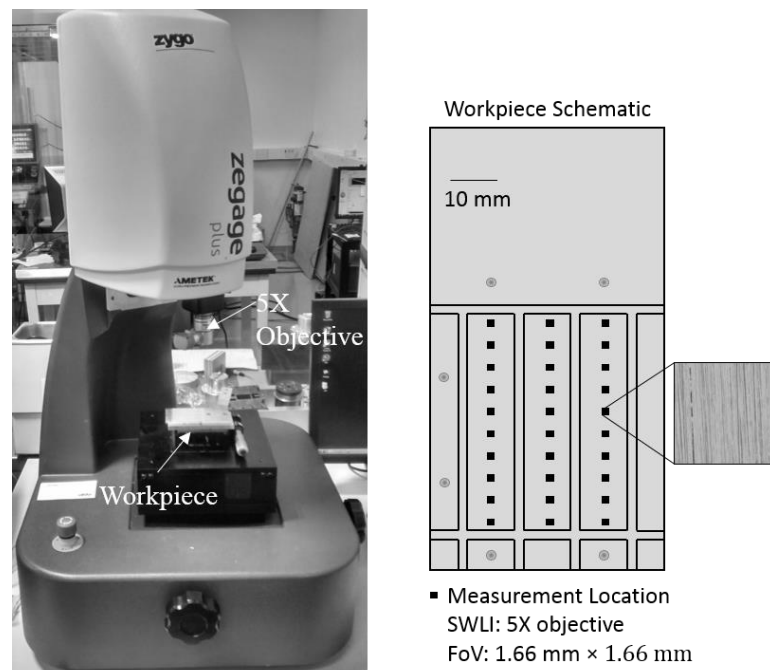


Figure 4.9 (Left) Zygo ZeGage SWLI. (Right) Measurement locations.

To ensure that the pre- and post-finishing measurements were taken approximately at the same locations, a fixture that combined the movements of a linear stage (Thorlabs) and a rotary stage (Newport 481-A) is used to align the workpiece with the reference position on the SWLI instrument (see Figure 4.10 for fixture details).

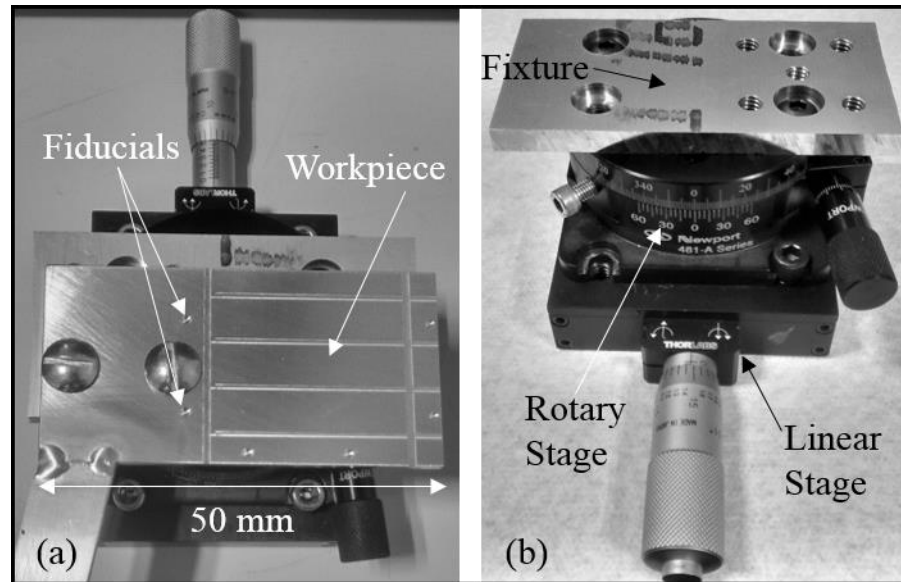


Figure 4.10 Fixture for integrating linear and a rotary stage movements to align workpiece position

4.8 Surface finishes on aluminum workpieces

The data acquired from SWLI measurements and described in section 4.7 is processed in MATLAB® R2016b and Zygo ZeGage Mx software and the surface finishes are quantified by evaluating RMS roughness (Sq) and texture aspect ratio (Str) from the acquired height data (Sq value is calculated in MATLAB® R2016b and Str value is taken from the Zygo ZeGage Mx software). The form error in the acquired height data is removed by subtracting a fourth order polynomial and the waviness error is accounted for by selecting a cut-off wavelength of 0.8 mm. The changes in Sq and Str values after 90 minutes of processing can provide insights into how the surface has been modified due to effective vibratory finishing. The following sub-sections discuss about the changes in surface topography observed on all the workpiece surface after processing in the vibratory bowl.

4.8.1 Test 1 – Tangential flow (Left surface)

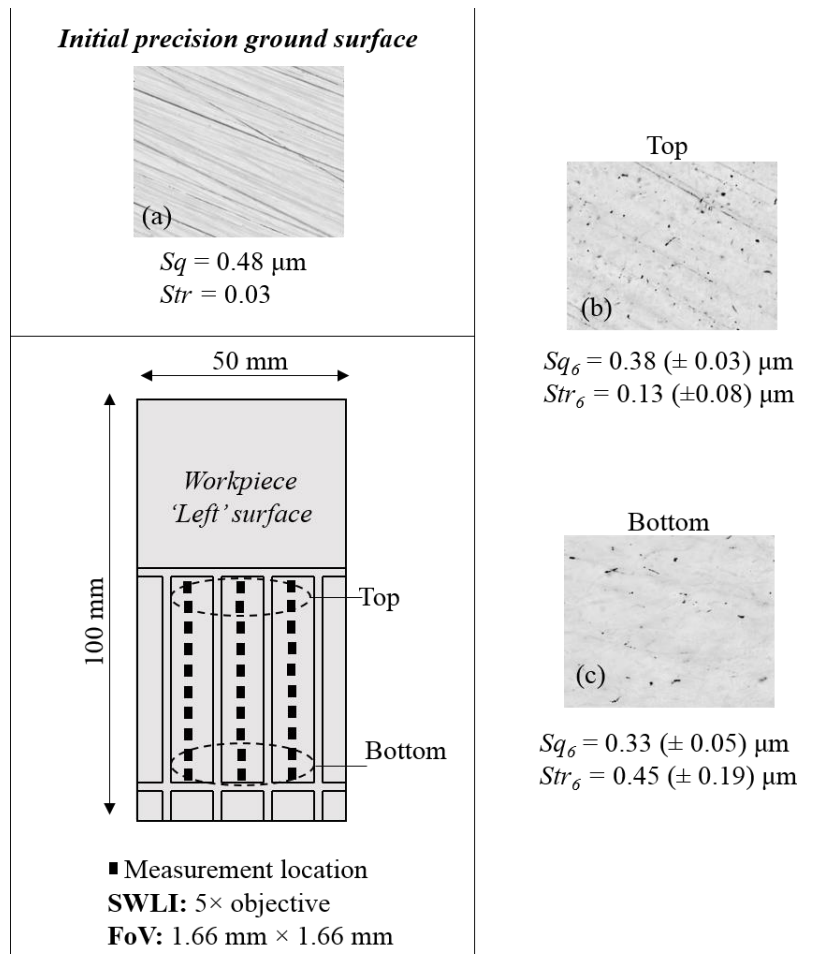


Figure 4.11 SWLI measurement on workpiece 'Left' surface for pre (a) and post Test 1 (b, c). See Figure 4.3 for workpiece surface naming convention

In Figure 4.11 (b) and (c), the reported Sq_6 and Str_6 are the average of six locations indicated in the lower left of Figure 4.11. The 'Left' surface experienced a decrease (or improvement) in the Sq value after finishing (initial Sq of $0.48 \mu\text{m}$ reduced to $0.38 \mu\text{m}$ near the top region after finishing, see Figure 4.11 (a) and (b), and near the bottom region it reduced to $0.33 \mu\text{m}$ after finishing, see Figure 4.11 (a) and (c)). The Str values obtained after finishing were in the range of 0.2 to 0.5 suggesting that an isotropic surface was not

generated even after 90 minutes of finishing. This can be verified by presence of grinding marks seen in Figure 4.11 (b).

4.8.2 Test 1 – Tangential flow (Right surface)

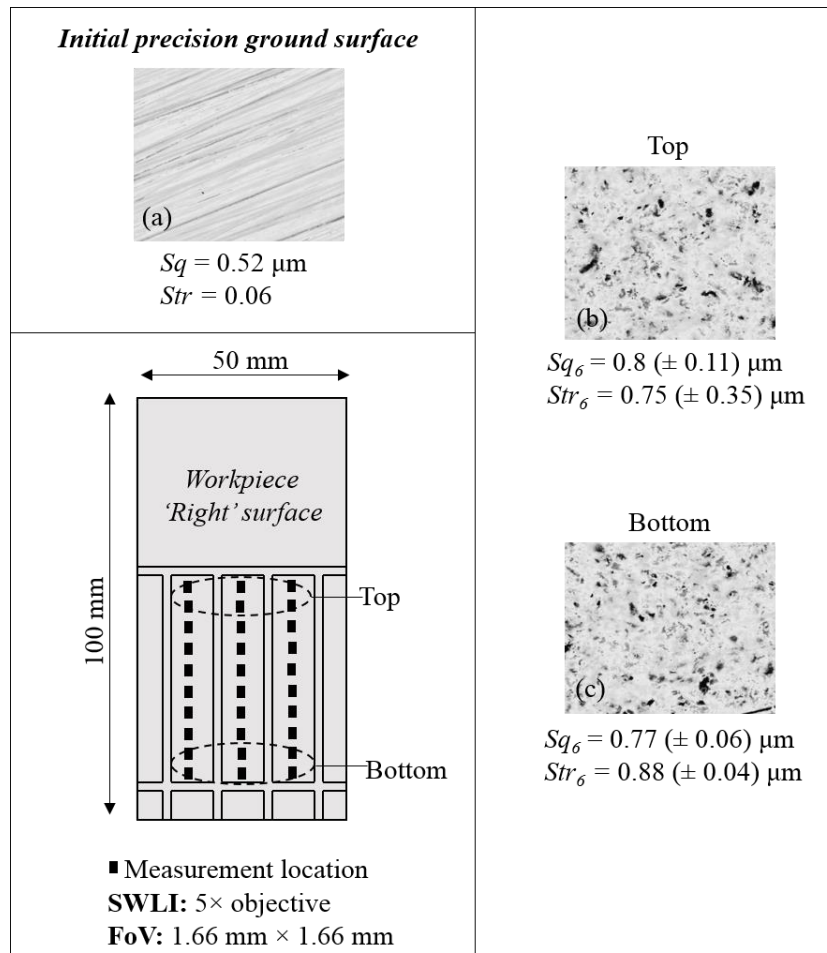


Figure 4.12 SWLI measurement on workpiece 'Right' surface for pre (a) and post Test 1 (b, c) indicating highest amount of pitting. See Figure 4.3 for workpiece surface naming convention

In Figure 4.12 (b) and (c), the reported Sq_6 and Str_6 are the average of six locations indicated in the lower left of Figure 4.12. The 'Right' surface experienced an increase (or deterioration) in the Sq values indicating that the surface turned rougher after 90 minutes of finishing. This is evident from the presence of the excessive pit marks seen in Figure 4.12 (b). The Str values obtained after finishing were in the range of 0.7 to 0.9. This

implicates that the surface obtained after finishing is non – directional and has an isotropic surface finish. This hold true as the grinding marks (indication of a highly directional surface) as seen on the initial precision ground surface (see Figure 4.12 (a)) were completely removed after workpiece finishing. This result is further investigated and flow conditions leading to this result are later discussed in chapter 5.

4.8.3 Test 2 – Normal flow (Upstream surface)

In Figure 4.13 (b) and (c), the reported Sq_6 and Str_6 are the average of six locations indicated in the lower left of Figure 4.13. Similar to Test 1 ‘Left’ surface, the Str values obtained after finishing were in the range of 0.1 to 0.3 suggesting that an isotropic surface was not generated even after 90 minutes of finishing. On the other hand, the Sq value obtained after finishing was lower than the value for initial ground surface (see Figure 4.13 (a) and (b)) as well as was lower than the value for the processed ‘Left’ surface (see Figure 4.11 (b) and Figure 4.13 (b)). This is indicative of workpiece surface smoothening because of vibratory finishing. This result suggests that the ‘Upstream’ surface underwent higher degree workpiece surface smoothening (i.e. improvement in Sq value) than the ‘Left’ surface and the difference in the flow conditions around these two surfaces is investigated and described in chapter 5. The Test 2 video revealed that a stagnation zone was developed near the workpiece ‘Upstream’ surface (meaning that the media velocity was near to zero and the media pieces were getting stacked up at this location).

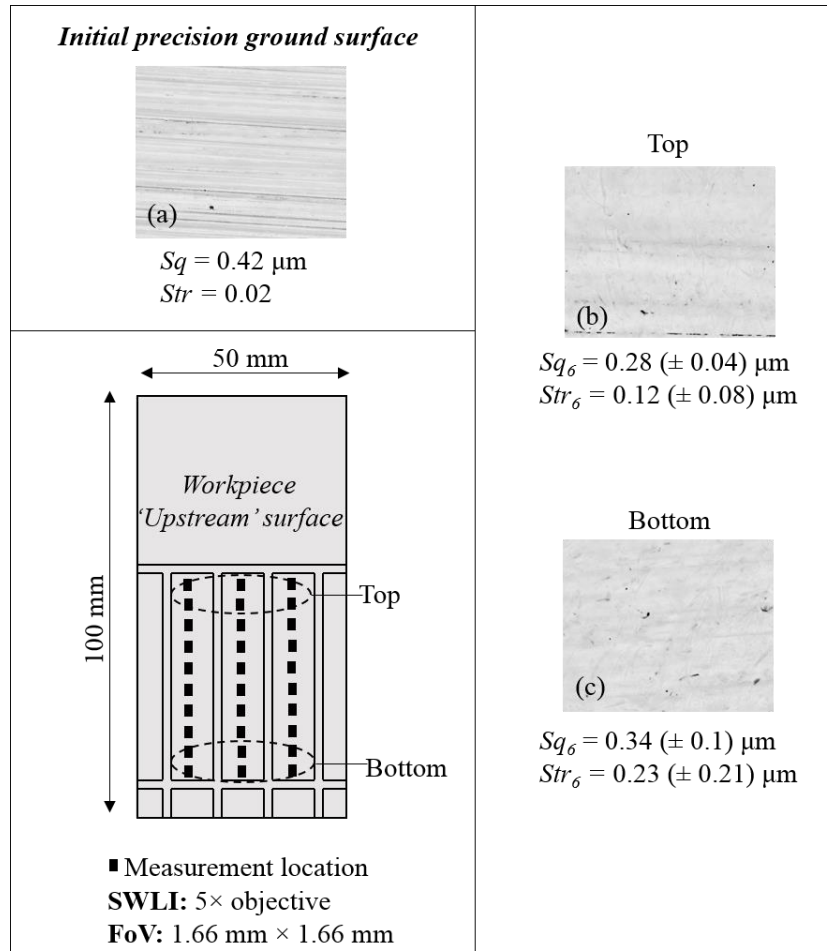


Figure 4.13 SWLI measurement on workpiece 'Upstream' surface for pre (a) and post Test 2 (b, c) indicating highest amount of surface smoothing. See Figure 4.3 for workpiece surface naming convention

4.8.4 Test 2 – Normal flow (Downstream surface)

In Figure 4.14 (b) and (c), the reported Sq_6 and Str_6 are the average of six locations indicated in the lower left of Figure 4.14. The 'Downstream' surface neither showed any signs of isotropic surface generation and nor did it undergo surface smoothing (i.e. improvement in Sq value) that is evident because of higher Sq values and near to zero Str values (see Figure 4.14 (b)). The Str values didn't change significantly change after finishing and were lower than 0.1 indicating presence of surface directionality which can be verified from Figure 4.14 (b). The SWLI measurement near the top region of the

‘Downstream’ surface showed no signs of media – workpiece interaction, i.e. this part of the surface was above the media free surface, and this is verified by subsequent playback of the video recorded by the high-speed imaging camera.

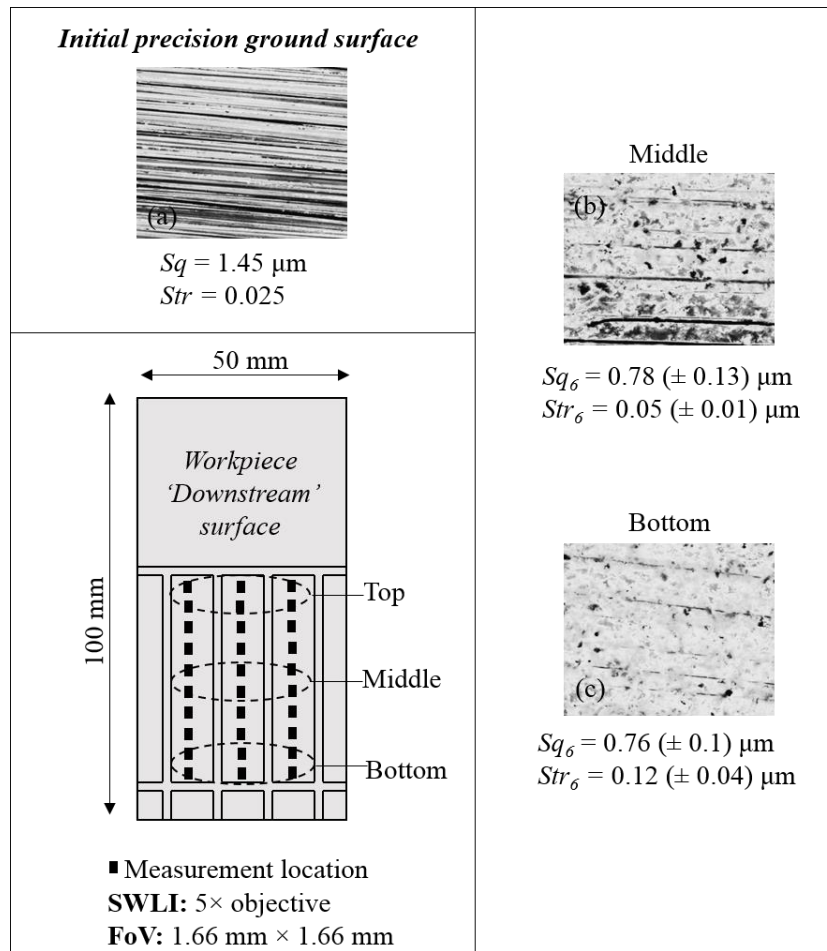


Figure 4.14 SWLI measurement on workpiece ‘Downstream’ surface for pre (a) and post Test 2 (b, c). See Figure 4.3 for workpiece surface naming convention

4.9 Summary

The generation of CFD model as outlined in chapter 3 was extended to model the flow of vibrating media around a stationary workpiece. A comparison between the CFD predicted velocities and the experimentally measured velocities approximately 5 mm from the workpieces surfaces exhibited a reasonable agreement as seen in Figure 4.7. Both, CFD

predicted and PIV measured velocities, are approximately 40 mm/s for tangential media flow and approximately 14 mm/s for normal media flow. The material removal in the two aluminum workpiece was quantified by measuring the average mass loss after finishing. For the two testing conditions implemented, i.e. tangential flow and normal flow condition, the average mass loss was 44 mg and 21 mg respectively, indicating that very little material was removed during finishing. This suggests that for the given media-workpiece combination surface modification is more prevalent. The resulting surface topography, evaluated by Sq and Str surface parameters obtained from SWLI, on the aluminum workpieces subjected to tangential near-workpiece and normally-impinging near-workpiece media flow was very different and the flow conditions leading to the distinct surface topologies are discussed in the following chapter.

5 CORRELATION BETWEEN CFD MODEL OUTPUTS AND RESULTING WORKPIECE TOPOGRAPHY

With a goal to understand the interaction between the media and the workpiece and in order to get insights into the resulting changes in workpiece surface topography, the CFD derived pressure and velocity fields are taken into consideration. The CFD model provides a significant leverage as it predicts the media flow dynamic pressure around the workpiece which is difficult to obtain through experimentation. This new information obtained from the model when combined with conventional abrasive wear knowledge can provide substantial insights into the material removal mechanism in vibratory finishing processes. Though a complete predictive model is beyond the scope of the present work, initial observations may lay down a strong foundation for developing such a model in future. The subsequent sections provide details about how the changes in surface topography (or surface finishes) correlate to the CFD metrics (i.e. pressure and velocity fields).

5.1 Static pressure and tangential velocity profiles for Test 1 (tangential flow)

For Test 1, the numerically computed pressure profiles in the vicinity of the two workpiece surfaces (i.e. Left and Right) are clearly distinct, see Figure 5.1 (b). The average pressure near the workpiece Left surface is ~ 9 Pa and that near the Right surface is ~ 239 Pa.

The magnitudes of tangential velocities on the other hand near the two workpiece surfaces are very similar (see Figure 5.1 (a)) with the average tangential velocity of ~ 43 mm/s.

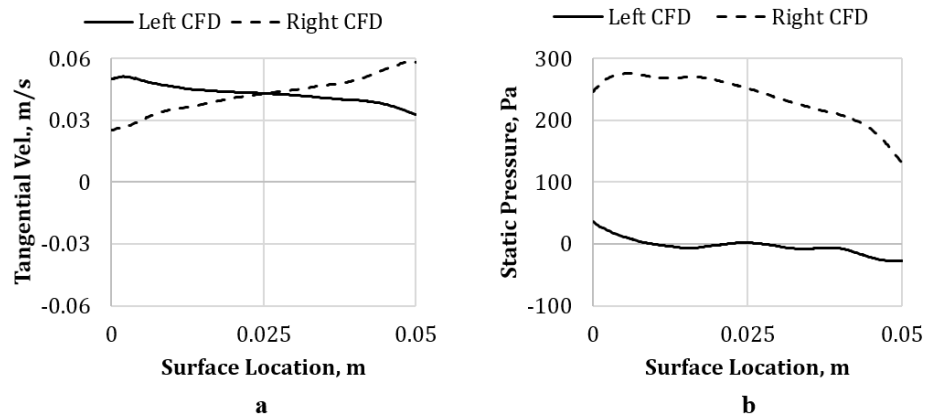


Figure 5.1 CFD predicted flow variables for Test 1. (a) Predicted tangential velocity, and (b) Predicted static pressure

5.2 Static pressure and tangential velocity profile for Test 2 (normal flow)

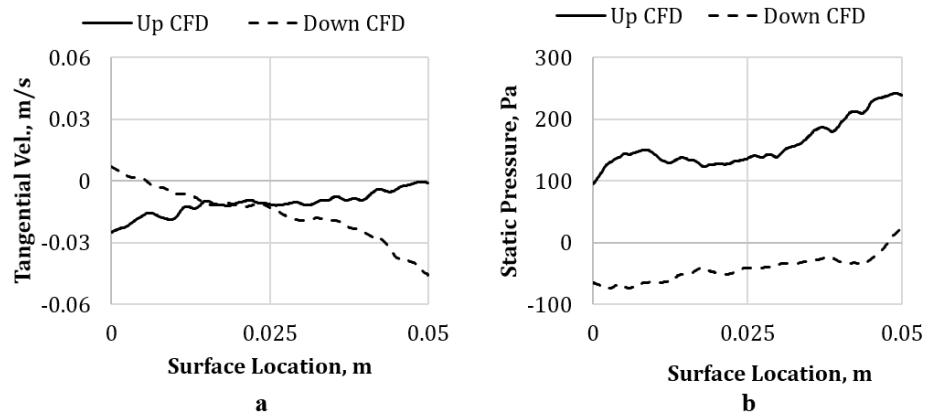


Figure 5.2 CFD predicted flow variables for Test 2. (a) Predicted tangential velocity, and (b) Predicted static pressure

Similar to Test 1, the numerically computed pressure profiles for the ‘Upstream’ and ‘Downstream’ surface are clearly distinct as seen in Figure 5.2 (b). The average pressure near the ‘Upstream’ surface is ~ 160 Pa and that near the ‘Downstream’ surface is ~ -43 Pa. The magnitudes of tangential velocities on the other hand near the ‘Upstream’

and ‘Downstream’ surface are very similar (see Figure 5.2 (a)) with the average tangential velocity of ~ 14 mm/s.

5.3 Correlation between CFD metrics and experimentally observed workpiece topographies

To investigate whether the CFD predicted pressures and time-averaged media velocities can provide insights into the process mechanics, changes in the surface topography as detailed in chapter 4, were considered with respect to the CFD outputs. While the outcomes are discussed in detail in a collaborative paper produced by the group [23], the main points are detailed here to indicate the importance of the effort expended in generating the CFD model outlined in chapter 3.

When the vibratory aspect of the process, the discrete nature of the media, along with its time averaged motion are considered, the different surface topologies can be explained. Test 1 ‘Right’ surface experiences the highest amount of pitting while Test 2 ‘Upstream’ surface shows signs of highest amount of surface smoothing. The predicted pressure and the velocity distributions existing around these two surfaces are analyzed to understand their effect on resulting surface topologies. These two surfaces (i.e. ‘Right’ and ‘Upstream’) experience the higher predicted fluid dynamic pressure (see Figure 5.1 (b) and Figure 5.2 (b)), however have a notably difference in the surface topographies. This, can be explained by taking both the tangential velocities and the vibrational impact of the media into consideration. For Test 1 ‘Right’, the average tangential velocity near the surface is ~ 43 mm/s. The process vibrations induced at the system’s driving frequency of 29 Hz along with the average tangential media velocity of ~ 43 mm/s leads to a media-workpiece contact every 1.4 mm (velocity/driving frequency). Of note here is that this distance is

within range of SWLI FoV (1.66 mm). This short duration well-separated media impact result in a highly pitted surface as seen in Figure 4.11 (b, c). Similarly, for Test 2 ‘Upstream’, the average tangential media velocity is ~ 14 mm/s. When the process vibrations along with the average tangential velocity are taken into consideration it is revealed that the media-workpiece contact occurs every ~ 0.5 mm. The subsequent surface smoothing (i.e. improvement in Sq value) as seen in Figure 4.12 (b) is due to the moderate flow pressure (~ 160 Pa) and slower progression of media at ~ 14 mm/s (contacting the workpiece surface every 0.5 mm) which results in a surface ploughing. The ‘Left’ and the ‘Downstream’ surface experience lower static pressures and show signs of pitting. The low Str values for these two surfaces suggests that isotropic surface finish was not achieved.

These findings suggest that CFD predicted flow conditions around the workpiece can provide insights into the distinct surface topographies expected under different processing conditions.

5.4 CFD based predictions to find optimal location of workpiece placement in the flow field

While experimental verification of the model under different conditions is beyond the scope of this work, the predicted CFD pressures and tangential velocities were determined when the workpiece is orientated at varied angles within the media flow. This provides insights on process sensitivity to workpiece orientation within the media.

The CFD model with boundary conditions as defined for Test 2 normal flow is considered for the study to determine how workpiece orientation with respect to the media flow affects the local media flow conditions. The workpiece orientation is changed from

0° to 160° as shown in Figure 5.3 (a) and the corresponding average predicted static pressure and average predicted tangential media velocity at approximately 5 mm from the two workpiece surfaces (i.e. 'Left' and 'Right', see Figure 5.3 (a)) are evaluated for each workpiece orientation (see Figure 5.3 (b) and (c)). From Figure 5.3 (b), it is observed that for a given workpiece orientation, higher predicted fluid dynamic pressures prevail around only one workpiece surface.

As higher fluid dynamic pressures combined with higher media flow velocities conditions are required for isotropic surface finishes, these results suggest that the workpiece orientation within the media flow would have to be changed to obtain an isotropic finish on all surfaces. The predicted fluid dynamic pressures and tangential media velocities around workpiece 'Left' surface are higher for workpiece inclined at 0° while the predicted fluid dynamic pressures and tangential media velocities around workpiece 'Right' surface are higher for workpiece inclined at 160° . Thus for obtaining an isotropic surface finish on the both the workpiece surfaces (i.e. Left and Right), the workpiece must be held stationary within the media flow at two distinct configurations: one where it is inclined at 0° and the other where it is inclined at 160° with respect to media flow.

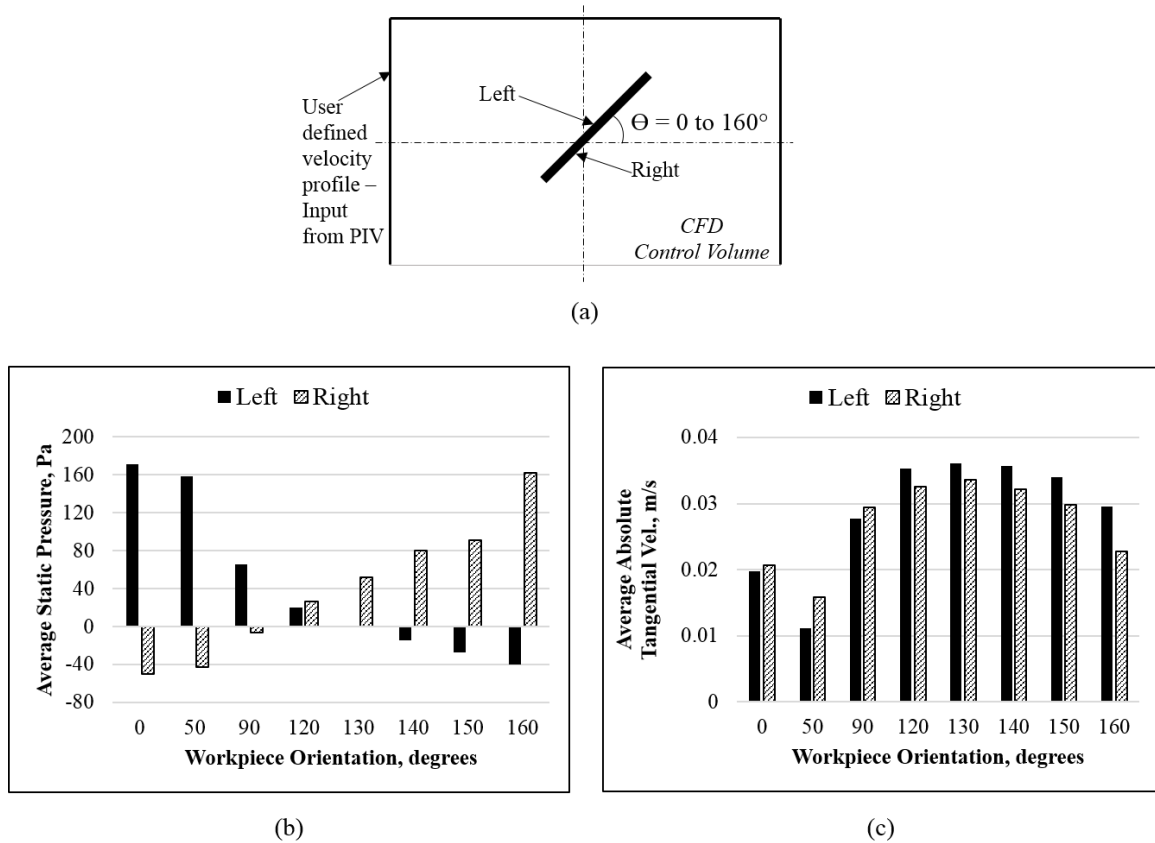


Figure 5.3 a) Workpiece surface naming convention and workpiece orientation, b) CFD derived average static pressure at approximately 5 mm from workpiece surface for a given workpiece orientation, and c) CFD derived average tangential velocity at approximately 5 mm from workpiece surface for a given workpiece orientation.

5.5 Media-workpiece contact model to investigate surface features obtained after finishing

The surface features observed on aluminum workpieces subjected to different media flow approach angles in a bowl-type vibratory finishing machine are investigated in order to gain insights into the media-workpiece interaction occurring during vibratory finishing. A notable difference in the workpiece surface topography is observed for tangential (i.e. Test 1) and normally-impinging (i.e. Test 2) near-workpiece media flow conditions. The former testing condition (i.e. tangential near-workpiece flow) results in high amount of pitting and an explanation for this is due to the workpiece experiencing well-separated short duration cyclic media impacts. The pitted surface topography as a

result of media impact can be viewed as a randomized indentation event where the media plastically deforms the workpiece surface. With a goal to develop an understanding of media-workpiece contact mechanism, an idealized case of a single asperity (i.e. granular media) loaded against a rigid plane surface (i.e. fixed workpiece surface) is considered. Although in reality, randomized contacts between large number of asperities (i.e. granular media) and the workpiece occur during vibratory finishing, the results derived for this idealized case can be extended further to analyze more complex cases as seen in most of loose abrasive processes.

Test 1 ‘Right’ surface (see Figure 5.4 for naming convention) shows evidence of excessive pitting which is attributed to presence of higher fluid dynamic pressure combined with higher tangential media flow velocity predicted by the CFD model, and well-separated short duration media impacts. To gain insights on how the media-workpiece interaction results in a heavily pitted surface, a theoretical contact model that assumes the media-workpiece contact as a contact between a sphere and a plane is implemented. Here the edge of the media that is in contact with the workpiece surface is assumed to be a rigid sphere. The CFD predicted average force exerted by the media on the workpiece surface along with the media geometry is correlated with the depth of pit marks obtained during processes.

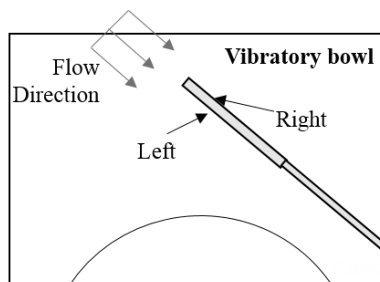


Figure 5.4 Test 1 - Tangential flow schematic and workpiece surface naming convention

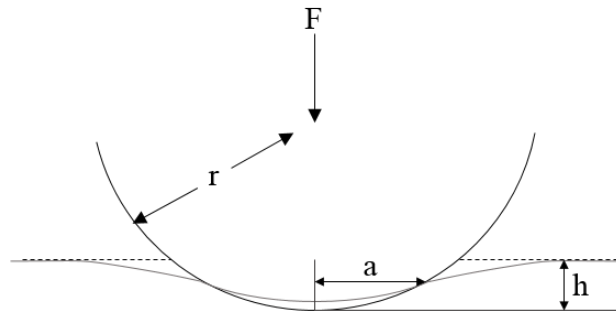


Figure 5.5 Indentation event created by media-workpiece contact

The radius of the media edge in contact with the workpiece, the normal load exerted by the media on the workpiece ‘Right’ surface, and their correlation to the depth of indentation are discussed below:

5.5.1 Radius of media edge

Figure 6.2 shows a schematic of contact between a single RSG 10/10 S media piece and the workpiece surface. Here, the edge of the media that is in contact with the workpiece is assumed to be a rigid sphere of radius r . The value of r is evaluated by acquiring a 3D height map of the media edge using a scanning white light interferometer (SWLI). Piston and tilt was removed from the subsequent measurement. Using the acquired 3D height map, a line profile is taken perpendicular to the length of the media edge (see Figure 6.2 (a)). The radius of the media edge is obtained by fitting an equation of a circle to the line profile and subsequent plot as seen in Figure 6.3 (b) gives the value for the radius, r . The value of r is obtained as $322.8 \mu\text{m}$.

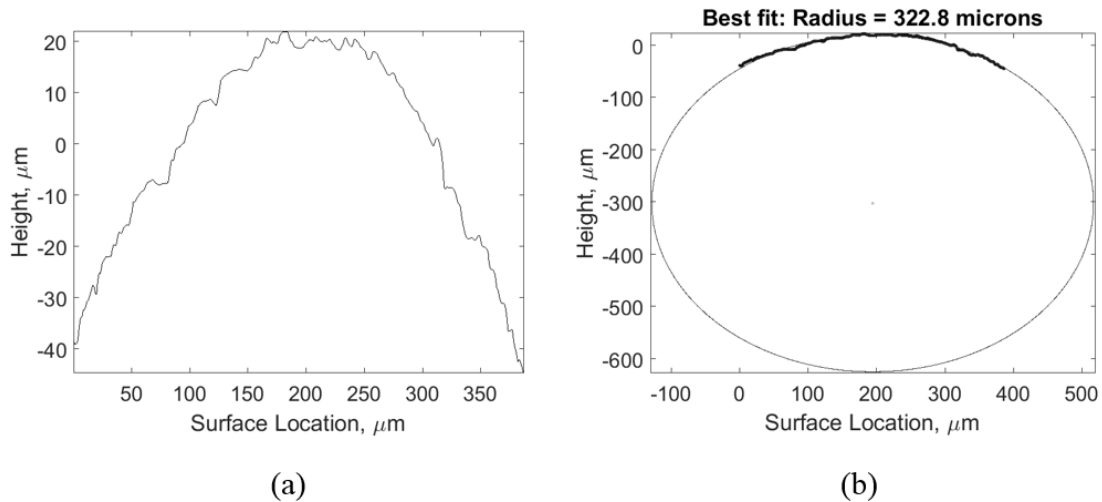


Figure 5.6 Evaluation of media edge radius. (a) line profile across the length of media edge obtained from SWLI measurement, and (b) Best-fit circle fitted to the line profile to obtain the media edge radius in μm

5.5.2 Normal load

The average force exerted on the workpiece ‘Right’ surface (see Figure 5.4 for naming convention) is predicted by the CFD model. This value also referred to as normal load is evaluated by the CFD software and is 2.625 N at the workpiece ‘Right’ surface. As a sanity check, this value is also validated by taking into consideration the average pressure predicted by the CFD model approximately 5 mm from the workpiece ‘Right’ surface. As described in section 5.1, the average pressure approximately 5 mm from the workpiece ‘Right’ surface is ~ 239 Pa. If this pressure is assumed to act uniformly over the entire workpiece surface area (i.e. $100\text{ mm} \times 50\text{ mm}$) then the force acting on the workpiece surface area is ~ 1.2 N. Of note here is that the hand-calculated force value (i.e. ~ 1.2 N) has the same order of magnitude as the CFD evaluated value (i.e. ~ 2.625 N). The difference can be attributed to the fact that hand-calculated force value is based on CFD predicted average pressure approximately 5 mm from workpiece surface while the CFD evaluated force value is at the workpiece ‘Right’ surface.

5.5.3 Empirical correlation

Figure 6.2 shows a schematic of a single piece of RSG 10/10 S media in contact with the workpiece surface. Here, r is the radius of the media edge in contact with the workpiece surface, F is the normal load exerted by the media on the workpiece surface, a is the radius of contact area (i.e. a circle) between the media and the workpiece, and h is the depth of indentation.

The radius a , of the circular contact area is given by the following equation by Hertz (1881) which is detailed in [25]:

$$a = \left(\frac{3Fr}{4E} \right)^{\frac{1}{3}} \quad (1.1)$$

Here E is an elastic modulus which depends on Young's moduli, E_{media} and $E_{workpiece}$, and on the Poisson's ratio, ν_{media} and $\nu_{workpiece}$ in the following way:

$$\frac{1}{E} = \frac{(1 - (\nu_{media})^2)}{E_{media}} + \frac{(1 - (\nu_{workpiece})^2)}{E_{workpiece}} \quad (1.2)$$

The material for the media is assumed to be aluminum oxide for which the value of Young's modulus is 300 GPa and the value for Poisson's ratio of 0.21. Thus the value of E_{media} is set equal to 300 GPa and the value for ν_{media} is set equal to 0.21. The Young's modulus for the workpiece (i.e. aluminum 6061), $E_{workpiece}$ is equal to 69 GPa and the Poisson's ratio, $\nu_{workpiece}$ is equal to 0.35. Substituting these values in Equation 1.2, gives the value for elastic modulus, E as 6.2878×10^{10} N/m². Consequently by substituting the value of elastic modulus, E in Equation 1.1, the value for the radius of contact area, a is obtained as 21.62 μ m.

The depth of indentation, h is given by the following equation:

$$a = \sqrt{rh} \quad (1.3)$$

Substituting the value of radius of contact area, a and radius of media edge, r the value for subsequent depth of indentation, h is evaluated as 1.448 μm .

5.6 Comparison of theoretical depth of indentation, h with the experimentally obtained depth of pit marks

Line profiles were traced along several pits that were observed on the 30 SWLI measurements taken on the ‘Right’ workpiece surface in order to estimate the depth of pits. Two out of the several line profiles, are considered to explain the procedure for evaluation of pit depth. The form error present in the areal SWLI measurement was removed by subtracting a plane and the waviness error was accounted for by selecting a high pass filter of 0.8 mm. The line profiles (0.5 mm trace) taken across two pit marks under consideration are shown in Figure 5.7 and Figure 5.8. The measurements labelled ‘Slice 1’ and ‘Slice 2’ are the line profiles taken across the two pits. From Figure 5.7 and Figure 5.8, it is seen that the pit depth obtained for ‘Slice 1’ is $\sim 3 \mu\text{m}$ while the pit depth obtained for ‘Slice 2’ is $\sim 1.5 \mu\text{m}$. Rest of the line profiles taken across several other pits were subjected to same surface processing parameters and the observed pit depth along these profiles ranged between $1 \mu\text{m} \sim 7 \mu\text{m}$. The purpose of these line profiles was to assess the variations in the pit depths and to check whether this depth is comparable to the indentation depth obtained from the theoretical model. To further validate the experimental pit depth, the surface PV values were taken into consideration. Though this is a very crude measure, the PV values provide a reference for the distance between the maximum (i.e. peak) and the minimum (i.e. valley) surface feature on the workpiece surface. The PV values for the 30 SWLI measurements on the workpiece ‘Right’ surface were in the range of $5 \sim 17 \mu\text{m}$.

5.7 Discussion of results

The theoretical depth of indentation (i.e. $\sim 1.5 \mu\text{m}$) caused by the media on the workpiece surface is comparable to the experimentally observed pit depths ($1 \sim 7 \mu\text{m}$). Of note here is that the theoretical model described in section 5.5 depicts a single asperity (i.e. single media piece) pressed against a rigid surface (i.e. fixed workpiece). In the real world, the nature of media-workpiece interaction can be described as a free-impact that occurs in a randomized manner. Unlike the idealized theoretical case where the media is pressed on the workpiece surface with some load N , in reality the media is travelling at a certain velocity before it impacts on the workpiece surface. Thus the differences in the theoretical and the experimental value can be attributed to the randomized impact nature of media, the assumption of media material properties, variations in average force predicted by the CFD model due to boundary conditions, and processing time of vibratory finishing.

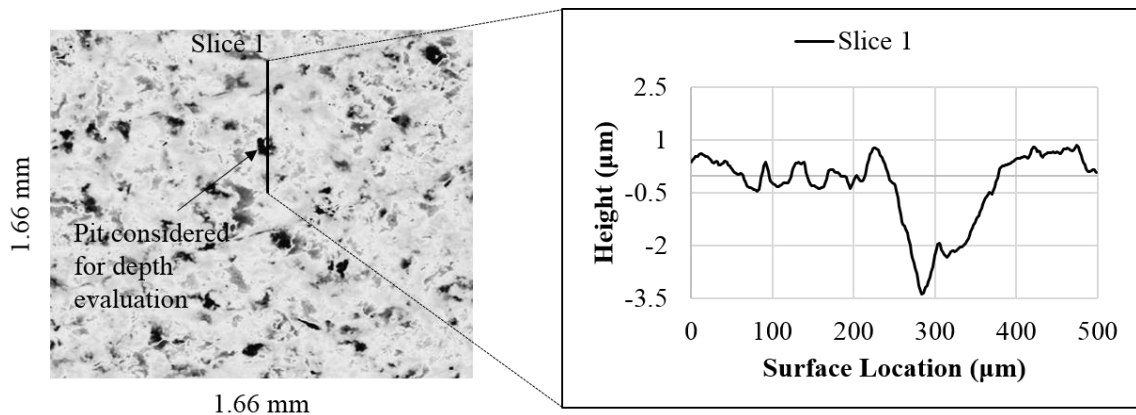


Figure 5.7 SWLI measurement of workpiece 'Right' surface. Slice 1 refers to a profile measurement across a 0.5 mm trace

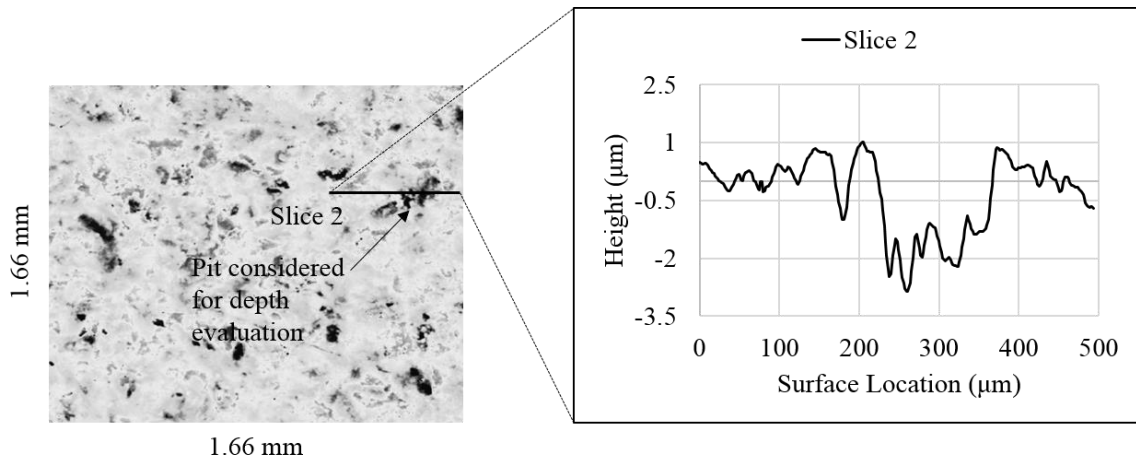


Figure 5.8 SWLI measurement of workpiece 'Right' surface. Slice 2 refers to a profile measurement across a 0.5 mm trace

5.8 Summary

The media flow conditions prevailing near the workpiece surfaces subjected to tangential near-workpiece flow and normally-impinging near-workpiece flow were investigated in order to gain insights into the surface finishes obtained after finishing. It was observed that the presence of higher fluid dynamic pressures combined with higher media tangential velocities near the workpiece promotes an isotropic finish, that is more pitted than the original surface while moderate fluid dynamic pressures combined with slower media tangential velocities near the workpiece promotes ploughing and subsequent surface smoothening (i.e. improvement in S_q value). CFD based predictions were implemented to identify the optimal location of workpiece placement within the media flow and it was realized that the workpiece orientation within the media flow would have to be changed to obtain an isotropic finish on all surfaces. Theoretical modelling of an idealized case of media-workpiece contact provided initial insights into the heavily pitted surface obtained after finishing.

6 CONCLUSIONS AND FUTURE WORK

6.1 Summary of work to date

A continuum mechanics based approach to model the flow of media around a stationary workpiece has been demonstrated in this work. Nontrivial implementation of the two-dimensional CFD model in ANSYS® FLUENT® delineating media flow conditions was realized by developing a methodology to extract velocity profiles from PIV measured time-averaged media velocity field, Chapter 3. These PIV based user defined velocity profiles serve as fundamental inputs to the CFD model, whereby they are input to the model via C programming language sub routines. Despite the fact that a simple two-dimensional model based on governing equations of continuum mechanics stipulated via Navier-Stokes equations [32] is used to numerically approximate the three-dimensional media flow field in a vibratory finisher, initial observations reveal that there is a reasonable agreement between the model-predicted and experimentally measured media velocity fields. The CFD derived media velocity field is approximately 5 % slower than the PIV measured velocity field near the three inlet boundaries, while it is 25 % slower than the PIV measured velocity field towards the outlet. The larger difference near the outlet is not unexpected as the media interacts with the inner wall of the bowl's annulus and takes on a complex 3D motion that is not captured in the 2D model. Thus if the workpiece is placed nearer to the velocity inlets then the CFD can provide realistic velocity field predictions. The CFD model was further extended to predict the media flow around a stationary workpiece, Chapter 4.

The predicted numerical approximation of media flow field around the stationary workpiece had reasonable agreement with the experimentally measured time-averaged media flow field. The velocity fields shared the same flow patterns, while the predicted velocity magnitudes 5 mm away from the workpiece surface were comparable to PIV measured values. Differences between the measured and predicted values can be attributed to the uncertainty in PIV measurements of the flow field and the simplification of three-dimensional media flow conditions to a two-dimensional flow model. Importantly, these observations corroborate the hypothesis that the vibrating media can be treated as a fluid. This new information enables commercially-available CFD software packages to be utilized to gain insights into vibratory finishing processes and thereby assist in making process predictions and characterization.

One potential benefit of using a CFD modeling approach is that it provides information on local pressure gradients in the vicinity of the workpiece. Continuous pressure profiles are very difficult to measure experimentally. As detailed in Chapter 5, when these CFD predicted local pressures and velocities are combined with knowledge of the system's vibrational frequency, and the discrete nature of the media, it appears to be feasible to explain the final topography of the workpiece surface. Experimental testing of aluminum workpieces subjected to different media approach angles revealed that an isotropic surface finish, but rougher finish, is achieved when there are higher fluid dynamic flow pressures combined with higher media flow velocities around the workpiece region. Presence of moderate fluid dynamic pressures and slower media velocities lead to effective surface smoothening (i.e. improvement in Sq value) but does not promote an isotropic surface generation. While this work is still in the early stages, these results suggest that

CFD can be an important tool in creating a fully predictive modelling tool, which when fully realized can provide substantial insights into vibratory finishing processes.

A simple, idealized case of single asperity in contact with a rigid plane was used to model the contact between a single piece of media and workpiece surface as an indentation event. The average pressure predicted by the CFD model along with workpiece surface area was used to calculate the normal load exerted by the media on the workpiece. Empirical correlations derived by Hertz were invoked to predict the depth of indentation (or a pit) caused by the media into the workpiece surface. The predicted indentation depth of $\sim 1.5 \mu\text{m}$ is comparable to a sample of pits measured using the SWLI, i.e. $1 \mu\text{m}$ to $7 \mu\text{m}$. This approach could conceivably be used in combination with the steady state time averaged information obtained from the CFD model to provide a more comprehensive model that also considers media sizes and workpiece properties.

6.2 Future work

Section 5.4 illustrated how the local CFD predicted pressures and tangential velocities vary for the workpiece orientation (angles from 0° and 160°) within the media flow. Experimental work should be carried out to verify that the process outputs (i.e. surface finishes) vary accordingly. This approach could be further extended for workpieces with varied, more complex geometries. The current 2D CFD model depicts media flow at a surface level inside the vibratory finisher. A natural extension of this model is to develop a 3D model that captures the circulatory nature of the media in the container. While the material removal rates achieved in the current set up were low, all the procedures exist for measuring material removal uniformity across workpiece surface. A media-workpiece combination that produces higher material removal rates should be found and the tests re-

run. The CFD model outputs can then be considered with respect to the material removal rates and material removal profiles; thus providing even more industrially relevant process insights. Further developments in the model will involve combining the time-averaged media flow with the discrete stochastic vibration based media-workpiece contact in order to provide a complete process model. The future modelling approaches will also include the material properties of media and the workpiece in the analysis.

PUBLICATION

1. B. Mullany, H. Shahinian, J. Navare, F. Azimi, E. Fleischhauer, P. Tkacik, R. Keanini, The application of computational fluid dynamic to vibratory finishing processes, Accepted for publication in the Annals of the CIRP, 66(1), 2017.

REFERENCES

1. Gillespie, L.R. and I. Press, *Mass Finishing Handbook*. 2006: Industrial Press.
2. Azimi, F., Fleischhauer, E., Tkacik, P., Keanini, R., Mullany, B., *Correlations between media-workpiece contact modes occurring during vibrational finishing and the resulting workpiece topography*, in *15th International Conference on Metrology and Properties of Engineering Surfaces*. 2015: Charlotte, USA.
3. Kittredge, J., *Understanding Vibratory Finishing Revisited*. Products Finishing, 1998. **62**: p. 8.
4. Testing, A.S.f., et al., *Cleaning Stainless Steel: A Symposium*. 1973: American Society for Testing and Materials.
5. B. Mullany, E. Fleischhauer, F. Azimi, P. Tkacik, R. Keanini, *Vibrational Finishing Process Insights Made Possible By Particle Image Velocimetry*.
6. Sofronas, A. and S. Taraman, *Model development and optimization of vibratory finishing process*. International Journal of Production Research, 1979. **17**(1): p. 23-31.
7. Fleischhauer, E., et al., *Application of particle image velocimetry (PIV) to vibrational finishing*. Journal of Materials Processing Technology, 2016. **229**: p. 322-328.
8. Hashimoto, F. and D.B. DeBra, *Modelling and Optimization of Vibratory Finishing Process*. CIRP Annals - Manufacturing Technology, 1996. **45**(1): p. 303-306.
9. Mediratta, R., K. Ahluwalia, and S.H. Yeo, *State-of-the-art on vibratory finishing in the aviation industry: an industrial and academic perspective*. The International Journal of Advanced Manufacturing Technology, 2016. **85**(1): p. 415-429.
10. Uhlmann, E., A. Dethlefs, and A. Eulitz, *Investigation of Material Removal and Surface Topography Formation in Vibratory Finishing*. Procedia CIRP, 2014. **14**: p. 25-30.
11. Wang, S., R.S. Timsit, and J.K. Spelt, *Experimental investigation of vibratory finishing of aluminum*. Wear, 2000. **243**(1-2): p. 147-156.
12. Domblesky, J., V. Cariapa, and R. Evans, *Investigation of vibratory bowl finishing*. International Journal of Production Research, 2003. **41**(16): p. 3943-3953.
13. Ahluwalia, K., R. Mediratta, and S. Yeo. *Experimental Investigation of Fixtured Vibratory Finishing*. in *Proceedings of the World Congress on Engineering*. 2016.

14. Ahluwalia, K., R. Mediratta, and S.H. Yeo, *A novel approach to vibratory finishing: Double vibro-polishing*. Materials and Manufacturing Processes, 2016: p. 1-6.
15. Domblesky, J., R. Evans, and V. Cariapa, *Material removal model for vibratory finishing*. International Journal of Production Research, 2004. **42**(5): p. 1029-1041.
16. Hashimoto, F., S.P. Johnson, and R.G. Chaudhari, *Modeling of material removal mechanism in vibratory finishing process*. CIRP Annals - Manufacturing Technology, 2016. **65**(1): p. 325-328.
17. Prakasam, P.K., S. Castagne, and S. Subbiah, *Mechanism of Surface Evolution in Vibratory Media Finishing*. Procedia Manufacturing, 2015. **1**: p. 628-636.
18. Uhlmann, E., A. Dethlefs, and A. Eulitz, *Investigation into a geometry-based model for surface roughness prediction in vibratory finishing processes*. The International Journal of Advanced Manufacturing Technology, 2014. **75**(5): p. 815-823.
19. Yabuki, A., M.R. Baghbanan, and J.K. Spelt, *Contact forces and mechanisms in a vibratory finisher*. Wear, 2002. **252**(7-8): p. 635-643.
20. Baghbanan, M.R., et al., *Tribological behavior of aluminum alloys in a vibratory finishing process*. Wear, 2003. **255**(7-12): p. 1369-1379.
21. Ciampini, D., M. Papini, and J.K. Spelt, *Impact velocity measurement of media in a vibratory finisher*. Journal of Materials Processing Technology, 2007. **183**(2-3): p. 347-357.
22. Keanini, R.G., et al., *Macroscopic liquid-state molecular hydrodynamics*. Scientific Reports, 2017. **7**: p. 41658.
23. B. Mullany, H. Shahinian, J. Navare, F. Azimi, E. Fleischhauer, P. Tkacik, R. Keanini, *The application of computational fluid dynamics to vibratory finishing processes*. CIRP Annals - Manufacturing Technology, 2017. **66**(1).
24. Wan, S., *A Framework for the Analysis of Mass Finishing Processes*. 2012.
25. Hutchings, I.M., *Tribology: Friction and Wear of Engineering Materials*. 1992: Edward Arnold.
26. Wan, S., T. Sato, and A. Hartawan. *Vibratory finishing of immobilized cylinders*. in *Advanced Materials Research*. 2012. Trans Tech Publ.
27. Adrian, R.J. and J. Westerweel, *Particle Image Velocimetry*. 2011: Cambridge University Press.
28. Anderson, J., *Computational Fluid Dynamics*. 1995: McGraw-Hill Education.

29. Mayes, C., et al., *Boundary-Layer Theory*. 2003: Springer Berlin Heidelberg.
30. Patankar, S., *Numerical Heat Transfer and Fluid Flow*. 1980: Taylor & Francis.
31. ISO25178-2, *Geometrical product specification (GPS) - Surface texture: Areal - Part 2: Terms, definitions, and surface texture parameters*. 2012.
32. Temam, R., *Navier-stokes equations*. Vol. 2. 1984: North-Holland Amsterdam.

APPENDIX A: MATLAB CODE TO EXTRACT MEDIA VELOCITY FIELD FROM PIV RAW DATA

```

clear all;
clc;
name = 'tanflowplate_redo_sample2'; %selecting file containing PIV raw
data
name = strcat(name, '.mat');
load(name); %load PIV raw data in Matlab
su=0;
sv=0;
dx = 3.5; %PIV spatial resolution in 'x' direction (mm)
dy = 3.5; %PIV spatial resolution in 'y' direction (mm)

for i=1:length(Input{1}.dataset)
    ux=Input{1}.dataset(i).U;
    vy=Input{1}.dataset(i).V;
    su=su+ux;
    sv=sv+vy;
end
vel_u=su/length(Input{1}.dataset); %extracting 'X' velocity from PIV
raw data
vel_v=sv/length(Input{1}.dataset); %extracting 'Y' velocity from PIV
raw data
V_mag=sqrt(vel_u.^2+vel_v.^2); %evaluating the velocity magnitude
[ny,nx]=size(vel_u);
xm = (0:1:nx-1)*dx;
ym = flipud((0:1:ny-1)*dy);
[X,Y]=meshgrid(xm,ym);
scale_factor = 50; %define a factor to scale the velocity vectors for
better comparison
figure
q = quiver(X,Y,vel_u*scale_factor,vel_v*scale_factor);
axis([0 max(max(X)) 0 max(max(Y))])
xlabel('X (mm)');
ylabel('Y (mm)');
set(q, 'linewidth', 1);
set(gca, 'fontsize', 12, 'fontweight', 'demi');
saveas(gcf, 'vecplot.tif')

```

APPENDIX B: C PROGRAM TO LINK PIV VELOCITIES TO CFD MODEL

```

#include "udf.h"

DEFINE_PROFILE(top_xvel,thread,index)
{
  real x[ND_ND];
  real y;
  face_t f;

  begin_f_loop(f,thread)
  {
    F_CENTROID(x,f,thread);
    y=x[0];
    F_PROFILE(f,thread,index)=(insert equation for top inlet 'x' velocity);
  }
  end_f_loop(f,thread)
}

DEFINE_PROFILE(top_yvel,thread,index)
{
  real x[ND_ND];
  real y;
  face_t f;

  begin_f_loop(f,thread)
  {
    F_CENTROID(x,f,thread);
    y=x[0];
    F_PROFILE(f,thread,index)=(insert equation for top inlet 'y' velocity);
  }
  end_f_loop(f,thread)
}

DEFINE_PROFILE(left_xvel,thread,index)
{
  real x[ND_ND];
  real y;
  face_t f;

  begin_f_loop(f,thread)
  {
    F_CENTROID(x,f,thread);
    y=x[1];
    F_PROFILE(f,thread,index)=(insert equation for left inlet 'x' velocity);
  }
  end_f_loop(f,thread)
}

DEFINE_PROFILE(left_yvel,thread,index)
{
  real x[ND_ND];
  real y;
  face_t f;

```

```

begin_f_loop(f,thread)
{
  F_CENTROID(x,f,thread);
  y=x[1];
  F_PROFILE(f,thread,index)=(insert equation for left inlet 'y' velocity);
}
end_f_loop(f,thread)
}

DEFINE_PROFILE(right_xvel,thread,index)
{
  real x[ND_ND];
  real y;
  face_t f;

  begin_f_loop(f,thread)
  {
    F_CENTROID(x,f,thread);
    y=x[1];
    F_PROFILE(f,thread,index)=(insert equation for right inlet 'x' velocity);
  }
  end_f_loop(f,thread)
}

DEFINE_PROFILE(right_yvel,thread,index)
{
  real x[ND_ND];
  real y;
  face_t f;

  begin_f_loop(f,thread)
  {
    F_CENTROID(x,f,thread);
    y=x[1];
    F_PROFILE(f,thread,index)=(insert equation for right inlet 'x' velocity);
  }
  end_f_loop(f,thread)
}

```

APPENDIX C: MATLAB CODE TO EVALUATE SURFACE FINISHES FROM RAW BINARY FILE

```

clear all;
close all;
clc;

%import SWLI data into Matlab
for k = 1:30
fname = 'Al6061_2t_Zg5_p1_'; %filename without .dat extension and
measurement location
m = sprintf('%03d',k); %measurement location
filename = strcat(fname,m);
ext = '.dat'; %extension
name = strcat(fname,m,ext); %filename
Z = ReadZygoBinary(name); %This is function to read Zegage files and is
available online
Z = inpaint_nans(Z); %This function removes nans and replaces with
neighbour approximation. It is available on mathworks website
dx = 1.67/1024; %spacing in x in mm
dy = dx; %spacing in y in mm
x = linspace(0,1.67,1024); %x coordinates of field of view
y = linspace(0,1.67,1024); %y coordinates of field of view
[X,Y] = meshgrid(x,y);

%fitting a 4th order polynomial to raw data
ft = 'poly44';
fitresult = fit_polynomial(X,Y,Z,ft);
form = fitresult(X,Y);
Z1 = Z-form; %form removal

%applying 3D Gaussian filter
nx = 1024; %number of points along x
ny = 1024; %number of points along y
alpha = sqrt(log(2)/pi);
lambdacX = 0.8; %cut-off along x in mm
lambdacY = 0.8; %cut-off along y in mm
xa = (-lambdacX:dx:lambdacX-dx)';
ya = (-lambdacY:dy:lambdacY-dy)';
mx = size(xa,1);
my = size(ya,1);
for i = 1:mx
    for j = 1:my
        S(j,i) = (1/(alpha^2*lambdacX*lambdacY))*exp(-
pi*(x(i)/alpha/lambdacX)^2-pi*(y(j)/alpha/lambdacY)^2);
    end
end
S = S/sum(sum(S));
C = conv2(Z1,S);
w = C(my/2+1:ny+my/2,mx/2+1:nx+mx/2); %waviness
Z2 = Z1-w;

%Average roughness
Sa = mean(mean(abs(Z2)));

```

```
Sa = Sa*10^6;
Sa = sprintf('%0.2f',Sa);

%Rms roughness
Sq = rms(rms(abs(Z2)));
Sq = Sq*10^6;
Sq = sprintf('%0.2f',Sq);

%plotting the waviness removed height data
figure('visible','off')
imagesc(x,y,Z2*10^6)
set(gca,'YDir','normal')
cb3 = colorbar;
cb3.Label.String = 'Height (\mum)';
xlabel(['Sa = ' num2str(Sa) ' \mum, Sq = ' num2str(Sq) ' \mum'])
caxis([-3 3])
colormap(jet)
set(gca,'FontSize',18,'FontWeight','demi')
saveas(gcf,filename,'tif')

end
```

APPENDIX D: MATLAB CODE TO COMPARE CFD PREDICTED AND PIV MEASURED VELOCITIES

```

clc;
clear all;
close all;

%Loading CFD data
w = 0.187; %FOV width in m
h = 0.102; %FOV height in m
ia = 0.0034;%length of interrogation area in m
y = -h/2:ia:h/2;%y coordinates for curve fitting
xvel = zeros(length(y),56); %initialize media x velocity
yvel = zeros(length(y),56); %initialize media y velocity

%Extracting x and y velocities for 56 lines defined in corresponding
CFD model. Filename should be named as '1','2','3'...

for i=1:56
    m = dlmread(sprintf('%d', i), ',', 1, 0);
    m = sortrows(m, 3);

    for j=1:length(m)
        pos(j)=m(j, 3);
    end
    pos=(pos)';

    for k=1:length(m)
        u(k)=m(k, 4);
    end
    u=(u)';

    for l=1:length(m)
        v(l)=m(l, 5);
    end
    v=(v)';

    f1=spl_fit(pos,u);
    f2=spl_fit(pos,v);
    U=f1(y);
    V=f2(y);
    xvel(:,i)=U;
    yvel(:,i)=V;
end

mag = sqrt(xvel.^2+yvel.^2);
dir = atan(yvel./xvel);
xpos = (10.2:3.4:197.2)';
ypos = (34:3.4:136)';

figure(1)
q1 = quiver(xpos,ypos,xvel,yvel, 'k');
hold on

```

```

contour(xpos,ypos,mag,'linewidth',2);
cb = colorbar;
cb.Label.String = 'Velocity (m/s)';
xlabel('X (mm)');
ylabel('Y (mm)');
title('CFD velocity vector plot for RSG 10/10S')
set(q1,'linewidth',1);
set(gca,'fontsize',12,'fontweight','demi');

%loading PIV data into MATLAB
name = 'tanflow_redo_sample2';
name = strcat(name, '.mat');
load(name);
su = 0;
sv = 0;
dx = 3.4;%increments in mm
dy = 3.4;%increments in mm

for i = 1:length(Input{1}.dataset)
    ux = Input{1}.dataset(i).U;
    vy = Input{1}.dataset(i).V;
    su = su+ux;
    sv = sv+vy;
end
vel_u = su/length(Input{1}.dataset);
vel_v = sv/length(Input{1}.dataset);
a = vel_v(11:41,4:59);
b = vel_u(11:41,4:59);
V_mag = sqrt(b.^2+a.^2);
V_dir = atan(a./b);
[ny,nx] = size(vel_u);
xm = (3:1:nx-4)*dx;% x in mm
ym = flipud((10:1:ny-6)*dy);% y in mm
[X,Y] = meshgrid(xm,ym);

figure(2)
q2 = quiver(X,Y,b,a,'k');
hold on
contour(xpos,ypos,V_mag,'linewidth',2);
cb = colorbar;
cb.Label.String = 'Velocity (m/s)';
xlabel('X (mm)');
ylabel('Y (mm)');
title(' PIV velocity vector plot for RSG 10/10S')
set(q2,'linewidth',1);
set(gca,'fontsize',12,'fontweight','demi');

%comparison of PIV and CFD data
err_mag = V_mag-mag;
err_dir = ((a.*xvel)-(yvel.*b))./((b.*xvel)+(a.*yvel));
perr_mag = ((V_mag-mag)./V_mag).*100;
perr_dir = ((V_dir-dir)./V_dir).*100;

figure(3)
c1 = contourf(xpos,ypos,err_mag);

```

```
xlabel('X (mm)');
ylabel('Y (mm)');
title('Comparison of PIV and CFD vector plots')
set(gca, 'fontsize', 12, 'fontweight', 'demi');
cf1 = colorbar;
cf1.Label.String = 'Error in velocity magnitude (m/s)';

figure(4)
c2 = contourf(xpos, ypos, err_dir);
xlabel('X (mm)');
ylabel('Y (mm)');
title('Comparison of PIV and CFD vector plots')
set(gca, 'fontsize', 12, 'fontweight', 'demi');
cf2 = colorbar;
cf2.Label.String = 'Error in velocity direction';

figure(5)
c3 = contourf(xpos, ypos, perr_mag);
xlabel('X (mm)');
ylabel('Y (mm)');
title('Comparison of PIV and CFD vector plots')
set(gca, 'fontsize', 12, 'fontweight', 'demi');
cf3 = colorbar;
cf3.Label.String = 'Percentage error in velocity magnitude (%)';

figure(6)
c4 = contourf(xpos, ypos, perr_dir);
xlabel('X (mm)');
ylabel('Y (mm)');
title('Comparison of PIV and CFD vector plots')
set(gca, 'fontsize', 12, 'fontweight', 'demi');
cf4 = colorbar;
cf4.Label.String = 'Percentage error in velocity direction (%)';
```

APPENDIX E: MATLAB CODE TO SEQUENTIALLY ARRANGE AS PER TIMESTAMP AND CONVERT HIGH SPEED IMAGES TO GRAYSCALE

```
clear all
clc

for x = -2530 : 2529

    if x<0
        imwrite(rgb2gray(imread(strcat('G:\Multimedia\PIV
Data\Sample1\TestSession\TestSession_003\Right
Side',sprintf('%07d',x),'.tif'),'.tif')),strcat('G:\Multimedia\PIV
Data\Sample1\TestSession\TestSession_003_grayscale\RSG1010S_tanflow_',s
printf('%04d',x+2530),'.tiff'));
    else
        imwrite(rgb2gray(imread(strcat('G:\Multimedia\PIV
Data\Sample1\TestSession\TestSession_003\Right
Side',sprintf('%06d',x),'.tif'),'.tif')),strcat('G:\Multimedia\PIV
Data\Sample1\TestSession\TestSession_003_grayscale\RSG1010S_tanflow_',s
printf('%04d',x+2530),'.tiff'));
    end
end
end
```

APPENDIX F: MATLAB CODE TO SAVE PIV PROCESSED DATA AS A MATLAB M-FILE

```
%Run this script inside Dynamic studio software  
pathname = 'G:\Multimedia\PIV Raw Data\';  
filename = 'tanflowredo.mat';  
save(strcat(pathname,filename));
```